Influenza-induced activation of recruited alveolar macrophages during the early inflammatory phase drives lung injury and lethality

Clarissa M Koch[1], Kishore R Anekalla[1], Yuan-Shih Hu[1], Jennifer M. Davis[1], Mark Ciesielski[1], Gaurav Gadhvi[2], Shang-Yang Chen[2], Margaret Turner[1], Yuan Cheng[1], Bria M Coates[1,3,4], Hiam Abdala-Valencia[1], Paul A Reyfman[1], Alexander V Misharin[1], GR Scott Budinger[1], Deborah R Winter[2±], Karen M Ridge[1,5±]

[1]Pulmonary and Critical Care Division, [2]Rheumatology Division, Department of Medicine, [3]Department of Pediatrics, Northwestern University Feinberg School of Medicine, Chicago, IL USA, [4]Ann & Robert H. Lurie Children's Hospital of Chicago, Chicago IL, [5]Department of Cell and Developmental Biology, Northwestern University Feinberg School of Medicine, Chicago, IL.

± Contributed equally to this paper

Corresponding author:

Karen M. Ridge, Ph.D.
Northwestern University
Feinberg School of Medicine
Division of Pulmonary and Critical Care Medicine
Simpson Querrey Biomedical Research Center
Department of Cell and Developmental Biology
303 E. Superior, 5-520
Chicago, IL 60611
Kridge@northwestern.edu
312-503-1648 – office

Abstract

Severe respiratory virus infections initiate a robust host immune response that contributes to disease severity. Immunomodulatory strategies that limit virus-initiated inflammation are of critical importance. In this study, we compared the host response to influenza A virus (IAV) infection in susceptible animals (wild-type, WT) to resilient mice (*Vimentin*$^{-/-}$ mice). We identified distinct gene expression patterns in recruited monocyte-derived alveolar macrophages (MoAMs) associated with three phases (Infiltrating, Early Inflammatory, Late Inflammatory) that evolve in sequence over the course of IAV infection. We report a core set of pro-inflammatory genes involved in the WT MoAM Early Inflammatory response that is suppressed in *Vim*$^{-/-}$ MoAMs. Moreover, we identify CEBPB, Jun-AP1, and IRF transcriptions factors as regulators of this attenuated inflammatory response. We performed causal experiments using bone-marrow chimeras to credential that *Vim*$^{-/-}$ MoAMs with suppressed pro-inflammatory genes confer protection from influenza-induced mortality in WT susceptible mice. Taken together, these data support the notion that vimentin plays a causal role in determining the pro-inflammatory function of recruited MoAMs and drives IAV-induced lung injury.

Introduction

Severe viral pneumonia due to influenza A virus (IAV) or severe acute respiratory syndrome coronavirus 2 (SARS-CoV-2) is characterized by the release of proinflammatory mediators that damage the alveolar epithelial and capillary barrier to cause acute respiratory distress syndrome (ARDS)[1, 2]. This points to the importance of a balanced and regulated immune response, where infection can be controlled while keeping tissue damage to a minimum. This hypothesis is clinically supported by a recent analysis of patients enrolled in the ARDSnet, in which patients with a hyperinflammatory endotype of ARDS, characterized in part by increased levels of circulating cytokines and chemokines, had worse clinical outcomes [3].

Shortly after IAV or SARS-CoV-2 infection, tissue-resident alveolar macrophages (TRAMs) are depleted, and monocytes are released from the bone marrow and recruited into the infected, injured lung [1, 4-6]. Upon entering the lung, these recruited monocytes, referred to as monocyte-derived alveolar macrophages (MoAMs), drive the immune response in humans and mice. MoAMs activate inflammatory signaling pathways in response to pathogen- or damage-associated molecular patterns (PAMPs or DAMPs) released from infected and dying cells [1, 3, 4, 7]. Preventing the recruitment of MoAMs into the lung by deleting CCR2 or its ligand reduces the severity of the dysregulated immune response (e.g., no cytokine storm) without affecting viral clearance [4]. These data suggest that recruited MoAMs mediate the excessive pro-inflammatory response associated with tissue damage. Indeed, elevated levels of IL-1β and IL-18, cytokines produced by the NLRP3 inflammasome, in the alveolar exudate of IAV-infected patients serve as poor prognostic markers of viral pneumonia outcomes [8-10]. Inhibiting the NLRP3 inflammasome early in IAV infection impairs viral clearance and increases morbidity and mortality in mice [11]. In contrast, inhibiting the NLRP3 inflammasome post-viral clearance reduces inflammation-induced tissue damage and promotes lung repair [11, 12]. These studies highlight the importance of understanding that recruited alveolar macrophages may play different roles in the virus-infected lung depending on the

79 stage of infection (e.g., pre- versus post-viral clearance). As a result, therapies that target recruited
80 MoAMs may be of interest [4, 13, 14]; however, no study has yet investigated the time-dependent
81 transcriptional signature and function of MoAMs in response to IAV infection.
82
83 Vimentin, a type III intermediate filament, is ubiquitously expressed in macrophages and plays a
84 role in several critical immune response processes. Vimentin expression is increased in COVID-
85 19 patients' lungs compared with healthy, control and COPD patients [15]. In patients with
86 ulcerative colitis and Crohn's disease, vimentin expression was also significantly increased in
87 inflamed tissues [16]. Consistent with these observations, vimentin-null (*Vim*$^{-/-}$) mice develop
88 significantly less gut inflammation compared to wild-type mice with acute colitis induced by dextran
89 sodium sulfate [17]. We have shown that *Vim*$^{-/-}$ mice are protected from LPS-induced lung injury
90 and death by suppressing pro-inflammatory cytokines [18]. Vimentin is a known ligand for some
91 PRRs, including nucleotide-binding oligomerization domain-containing protein 2 (NOD2) and NLR
92 Family Pyrin Domain Containing 3 (NLRP3). We, and others, reported that vimentin is required to
93 activate the NLRP3 inflammasome [18, 19] and subsequent NF-κB activation [20], which is
94 consistent with the observation that pro-inflammatory gene expression is altered in microglia lacking
95 vimentin in a murine model of Alzheimer's disease [21]. Interestingly, bulk RNA-seq transcriptomic
96 analysis showed significant upregulation of *Vim*, which was associated with decreased viral host
97 resistance in cultured embryonic stem cells and embryos [22]. Collectively, these studies support
98 the notion that vimentin may play a role in the immune response to IAV infection.
99
100 The temporal transcriptional response of recruited MoAMs that drives the immune response in the
101 IAV-infected host has not been previously reported. For the first time, our data identifies the distinct
102 gene expression patterns in recruited MoAMs associated with three phases (Infiltrating, Early
103 Inflammatory, Late Inflammatory) that evolve in sequence following infection with influenza A virus.
104 Additionally, we report that wild-type mice mount a sustained pro-inflammatory response

contributing to increased lung injury and death. In contrast, *Vim*$^{-/-}$ mice are remarkably resilient to IAV infection. Whether vimentin plays a causal role in determining the pro-inflammatory function of recruited MoAMs in the IAV-infected lung has not been previously investigated. If vimentin indeed affects MoAMs' pro-inflammatory function, is it a cell-autonomous phenomenon? Using isochronic adoptive MoAM transfer experiments and molecular profiling in mice, we sought to determine whether the loss of vimentin-related protection from influenza-induced lung injury is intrinsic to *Vim*$^{-/-}$ MoAMs. Our data supports a paradigm in which recruited MoAMs upregulate vimentin expression, activate maladaptive responses, and consequently exhibit a persistent pro-inflammatory response, promoting virus-induced lung injury.

Results

Vimentin null mice are protected from influenza-induced lung injury and mortality

Our group has recently reported that persistent inflammation in patients with severe SARS-CoV-2 pneumonia is sustained via stable circuits between recruited alveolar macrophages and T cells[1]. Using single-cell RNA-seq, distinct clusters of monocytes-derived alveolar macrophages (MoAMs) were identified from the bronchoalveolar lavage fluid (BALF) collected from patients with severe SARS-CoV-2 pneumonia (**Figure 1a, Supplemental Figure 1a**) [1]. MoAM1 cluster was characterized by high expression of pro-inflammatory cytokine genes, including *IL1B, CXCL2, and CCL3,* and low expression of reparative genes *MRC1* and *C1QA* (**Figure 1c, d)** [23-25]. In contrast, cluster MoAM3 exhibited the highest expression of *MRC1, C1QA, and MERTK. MERTK* encodes a receptor necessary for phagocytosis of apoptotic cells – the uptake of apoptotic cells reduces the expression of pro-inflammatory cytokines and chemokines from macrophages. This process has been mechanistically linked to transcriptional responses leading to a change in macrophage phenotype from pro-inflammatory to reparative [26, 27] (**Figure 1c-d).** By querying this single-cell RNA-seq dataset, we found that *VIM* was among the genes differentially expressed between MoAM1 and MoAM3: with the highest expression in the pro-inflammatory MoAM1 population and

132 decreasing in the reparative MoAM3 population (**Figure 1b-c).** These data from patients with severe
133 SARS-CoV-2 pneumonia show that higher *VIM* expression is associated with a pro-inflammatory
134 MoAM phenotype in viral pneumonia, while lower levels of *VIM* expression characterize MoAMs
135 with a reparative phenotype. Importantly, these data suggest that there may be a causal
136 relationship between *VIM* expression and MoAM phenotype.
137
138 Next, we used a clinically relevant, causal murine model of viral pneumonia to determine whether
139 the host response to influenza A virus (IAV) infection is altered in *Vim*$^{-/-}$ mice compared to WT mice.
140 WT and *Vim*$^{-/-}$ mice were infected with a lethal dose of IAV (Strain A/WSN/1933 (H1N1), 200 pfu)
141 and assessed for morbidity and mortality. WT mice had a 100% mortality rate, whereas >80% of
142 the *Vim*$^{-/-}$ mice were alive 10 days post-infection (p.i.) (**Figure 1e**). By 14 days p.i., 50% of the
143 surviving *Vim*$^{-/-}$ mice had recovered from mild lethargy, coat ruffling, febrile shaking, and eye-
144 watering. *Vim*$^{-/-}$ mice exhibited a lower wet-to-dry lung weight ratio and decreased total protein
145 concentration in BALF than WT mice infected with IAV, indicating less damage to the alveolar-
146 capillary barrier (**Figure 1f-g**). Histopathological examination of IAV-infected *Vim*$^{-/-}$ mice lungs also
147 demonstrated less severe alveolar damage, characterized by reduced alveolar edema and less
148 lung tissue damage than in IAV-infected WT mice (**Figure 1h**). Vimentin-deficiency did not interfere
149 with IAV replication or clearance, as evidenced by comparable viral titers (**Figure 1i**) and similar
150 levels of the H1N1 viral RNA molecules, such as matrix protein 2, nucleoprotein, and
151 neuraminidase, which were detected in recruited MoAMs from WT and *Vim*$^{-/-}$ mice by RNA-seq
152 (**Supplemental Figure 1b**). These results show that *Vim*$^{-/-}$ mice are surprisingly resilient to IAV
153 infection with improved survival rates and decreased lung injury, independent of viral load.
154
155 The influx of immune cells into the airspace during IAV infection and the resulting production of pro-
156 inflammatory cytokines is a major driver of lung injury. We performed a systematic flow cytometric
157 analysis of whole-lung lysates to characterize the immune cell recruitment into the lungs

158 (**Supplemental figure 1c**). The number of tissue-resident alveolar macrophages (TRAMs) rapidly
159 decreased after IAV infection at a similar rate in both genotypes, with a more than 80% reduction
160 by 6 days p.i. (**Figure 1j**). MoAMs are typically not present in the alveolar compartment in normal,
161 healthy lung tissue at steady-state (e.g., 0 days p.i.). During IAV infection, monocytes are recruited
162 and rapidly differentiated into MoAMs in the lung parenchyma [5, 28]. WT and *Vim*$^{-/-}$ mice infected
163 with IAV recruited comparably increasing number of MoAMs into the lung from 2 days p.i. onward
164 (**Figure 1j**). Similarly, neutrophil recruitment peaked on day 3 p.i. in both genotypes (**Supplemental**
165 **Figure 1d**). Despite similar immune cell recruitment, *Vim*$^{-/-}$ mice had decreased levels of pro-
166 inflammatory cytokines and chemokines, such as IL-1β, TNFα, RANTES, MIP-2, MCP-1, and Type
167 I interferons IFNα/β, compared to WT mice following IAV infection (**Figure 1k**). In summary, wild-
168 type mice, but not *Vim*$^{-/-}$ mice, exhibited a pro-inflammatory phenotype in response to IAV infection.
169 As there was no difference in MoAM recruitment between genotypes, these data suggest that
170 vimentin plays an essential role in determining the pro-inflammatory function of MoAMs.
171
172 **Three distinct temporal patterns characterize the transcriptional response of MoAMs to**
173 **influenza A virus**
174 To investigate the response of WT MoAMs to IAV infection, we performed RNA-seq on flow-sorted
175 MoAMs to assess global gene expression profiles on 2, 3, 4, and 6 days p.i. (**Supplemental Figure**
176 **2a, 2b**). We identified 2623 differentially expressed genes over this time course and, using k-means
177 clustering, defined three clusters that correspond temporally to three phases of the IAV response:
178 Infiltrating (2 days p.i.), Early Inflammatory (3-4 days p.i.), and Late Inflammatory (6 days p.i.)
179 (**Figure 2a**).
180
181 The first cluster is characterized by genes with the highest expression in the **Infiltrating Phase** at
182 2 days p.i. (**Figure 2a-b, Supplemental Figure 2c**). Gene Ontology (GO) analysis finds this cluster

183 is enriched for genes associated with *cell migration* and *cell adhesion*, such as *Cx3cr1, Rock1,*
184 *Tln1, and Cxcl14* (**Figure 2c-d**), likely involved in transendothelial migration of leukocytes[29-32].
185 These results are consistent with the requirement for MoAMs to leave the vasculature and migrate
186 across the endothelium to reach the alveolar space soon after IAV infection. We also observed
187 genes in this cluster associated with the recruitment of lymphocytes, such as *Cd86,* MHC Class II
188 gene *H2-Aa,* and *Ccl8* (**Figure 2c-d, Supplemental Figure 2d**). Furthermore, our results suggest
189 that MoAMs may be proliferating during this phase due to the enrichment of GO processes, such
190 as *DNA replication initiation*, and the expression of cell cycle genes, such as *Mcm5* (**Figures 2c-f**).
191 Taken together, these data show that the primary role of MoAMs in the Infiltrating Phase of the IAV
192 response is to enter the lung parenchyma and promote the recruitment of immune cells.
193
194 The second cluster is characterized by genes that peak in expression during the **Early**
195 **Inflammatory Phase** at 3 days p.i. (**Figure 2a-b, Supplemental Figure 2c**). This cluster is
196 enriched for genes associated with *inflammatory response* and *regulation of cytokine secretion*
197 (**Figure 2c)** – such as *Tlr2*, *Il1b,* and *Il1r2* **(Figure 2d)**. These gene expression changes correspond
198 with the secretion of inflammatory cytokines, such as IL-1β and TNFα, beginning on Day 3 of IAV
199 response (**Figure 1k)** and binding of viral PAMPs through pattern recognition receptors (PRRs),
200 including TLR2 [28]. The expression of genes associated with *chemotaxis,* such as *Ccl3, Ccl2,* and
201 *Cxcl2,* also peak during the Early Inflammatory phase (**Figure 2c-d**) and corresponds with the
202 secretion of their respective proteins MCP-1, MIP1-α and MIP-2 measured in the BALF (**Figure**
203 **1k**). These data collectively suggest that WT MoAMs adopt a pro-inflammatory state during the
204 Early Inflammatory Phase of the IAV response.

205 The third cluster is characterized by genes that display a continuous increase in expression until
206 the **Late Inflammatory Phase** at 6 days p.i. (**Figure 2a-b, Supplemental Figure 2c**). This cluster
207 is enriched for genes associated with the GO processes of *cell differentiation* and *adaptive immune*

208 *response* – such as *Irf8, Mafb, Ifng, Ctsh, Ccr1* and*, Arg2* (**Figure 2d, Supplemental Figure 2d).**
209 The increasing expression of *Irf8* and *Mafb* further supports the notion that recruited monocytes
210 differentiate into monocyte-derived alveolar macrophages [33, 34]. Interestingly*,* the gene encoding
211 vimentin increased in expression over time, suggesting that vimentin may play a role throughout
212 the IAV response (**Figure 2d**). Although GO analysis implicated metabolic processes in this cluster
213 (**Figure 2c**), and macrophage activation has been associated with cellular respiration changes[35-
214 37], we did not observe preferential expression of genes in the glycolysis or oxidative
215 phosphorylation pathways at any time point (**Figure 2e-f**).

216

217 Since interferon pathways are an essential element of the viral immune response, we investigated
218 the temporal expression of Type I and Type II interferon genes. We found Type I IFNα response
219 genes peaked in expression on day 2, which coincided with their enrichment in the Infiltrating cluster
220 (**Figure 2e-f)**. This is also consistent with Type I IFNs' role in viral clearance. In contrast, Type II
221 IFNy response genes did not reach their highest expression level until 6 days p.i. and were enriched
222 in the Late Inflammatory cluster (**Figure 2d-f)**. Type II IFNy has been shown to stimulate
223 macrophages and monocytes to produce more chemoattractants and other inflammatory
224 molecules, resulting in a cycle of persistent inflammation [1, 38]. These data support Type I
225 interferon's role as an early effector of the immune response, while Type II interferon is involved in
226 the later immune response.

227

228 While GO analysis can be informative, many terms, such as *inflammatory response* and *innate*
229 *immune response,* lack cell-type specificity. *In vivo* macrophages are characterized by considerable
230 diversity and plasticity and respond to environmental cues by acquiring distinct functional
231 phenotypes. *In vitro* macrophages can be polarized toward a pro-inflammatory (M1) phenotype or

232 a reparative (M2) phenotype through the administration of LPS or IL-4, respectively [25, 39, 40]. To
233 further define the generic *inflammatory response* in recruited MoAMs, we generated annotations
234 for $M_{(LPS)}$ and $M_{(IL-4)}$ responses by integrating gene sets from several published studies on LPS
235 ($M_{(LPS)}$), and IL-4 ($M_{(IL-4)}$) stimulated macrophages *in vitro* (see Methods)[25, 39-41]. We found that
236 $M_{(IL-4)}$ genes were enriched in the Infiltrating cluster, and their expression peaked on day 2 p.i.
237 Notably, recruited WT MoAMs quickly downregulated $M_{(IL-4)}$ genes on days 3, 4, and 6 p.i. (**Figure**
238 **2e-f)**. Furthermore, we found that the $M_{(LPS)}$ genes peaked on day 3 p.i. in WT MoAMs **(Figure 2e**)
239 and were enriched in the Early Inflammatory cluster (**Figure 2f**). $M_{(LPS)}$ genes were also enriched
240 in the Late Inflammatory cluster (days 4 and 6 p.i.) but to a lesser degree. (**Figure 2f**). Taken
241 together, our results support a critical switch in WT MoAM function as they transition from their initial
242 transcriptional state in the Infiltrating phase to a pro-inflammatory phenotype during the Early and
243 Late Inflammatory phases.
244
245 ***Vim*$^{-/-}$ MoAMs modulate expression of Infiltrating and Early Inflammatory, but not Late**
246 **Inflammatory phase genes.**
247 To gain a better understanding of the conferred protection from IAV infection in *Vim*$^{-/-}$ mice (**Figure**
248 **1**), we performed RNA-seq on flow-sorted MoAMs from *Vim*$^{-/-}$ mice at 2, 3, 4, and 6 days p.i.
249 (**Supplemental Figures 2a, 2b, 3a**). We compared global gene expression between genotypes
250 each day p.i., identifying down- and upregulated genes in *Vim*$^{-/-}$ compared to WT MoAMs. The
251 greatest differential gene expression occurred on day 3 p.i. (**Figure 3a)**. To characterize processes
252 with differential expression between genotypes, we ran GO analysis on up- and downregulated
253 genes on each day p.i. (**Figure 3b**). Top GO processes that enrich on at least two days p.i. uncover
254 a pattern of downregulated expression of genes involved in the inflammatory response and stress
255 response and increased expression of genes involved in cell cycle and extracellular matrix
256 organization in *Vim*$^{-/-}$ MoAMs throughout IAV infection (**Figure 3b)**. Furthermore, using GSEA we
257 found that gene sets associated with inflammation – including $M_{(LPS)}$ and Type I Interferon – were

258 significantly decreased in expression in *Vim*$^{-/-}$ MoAMs on every day p.i. (**Supplemental Figure 3b)**,
259 In contrast, *Cell Cycle* and $M_{(IL-4)}$ associated genes had increased expression in *Vim*$^{-/-}$ MoAMs
260 compared to WT MoAMs (**Supplemental Figure 3b)**.
261
262 Using the prior clustering of 2623 genes across the three phases of the IAV response (**Figure 2a**),
263 we compared gene expression between MoAMs in WT and *Vim*$^{-/-}$ mice during each phase (**Figure**
264 **3c-e, Supplemental 3f-h**). In *Vim*$^{-/-}$ MoAMs, genes in the Infiltrating cluster were increased in
265 expression while genes in the Early Inflammatory cluster tended to be decreased (**Figure 3c,d,f,**
266 **Supplemental Figure 3g,h**). In contrast, genes in the Late Inflammatory cluster were less changed
267 between genotypes (**Figure 3e, Supplemental Figure 3g,h**). In line with our previous findings,
268 day 3 p.i. represented the most significant difference between genotypes in any cluster (**Figure 3c-**
269 **f**). Indeed, day 2 and day 3 *Vim*$^{-/-}$ MoAMs were globally more similar to each other than their WT
270 counterparts, suggesting a greater transcriptional shift occurs between day 2 to 3 p.i. in WT
271 compared to *Vim*$^{-/-}$ MoAMs (**Supplemental Figure 3f).** These transcriptional differences between
272 genotypes were mirrored in the data for processes associated with each phase (**Figure 2f**). $M_{(IL-4)}$
273 and Cell Cycle genes, associated with the Infiltrating phase, exhibited a higher and sustained level
274 of expression in *Vim*$^{-/-}$ MoAMs compared to WT (**Figure 3c**). These results were confirmed using
275 GSEA (**Supplemental Figure 3b**). Type I IFN response genes were differentially expressed
276 between genotypes, but were downregulated over time in both genotypes. In contrast, $M_{(LPS)}$ genes
277 associated with the Early Inflammatory phase were downregulated on 2 and 3 days p.i. in *Vim-/-*
278 compared to WT MoAMs (**Figure 3d**), suggesting an early attenuation. Type II IFN response gene
279 expression did not significantly differ between genotypes (**Figure 3e**). We next asked whether any
280 of the individual gene sets correlated with each other. We observed that $M_{(IL-4)}$ and Cell cycle gene
281 expression are highly correlated in both genotypes, suggesting they may be part of a more
282 extensive network of co-regulated processes (**Supplemental Figure 3c, d**). None of the gene sets
283 significantly differed in expression in steady-state tissue-resident alveolar macrophages,

284 suggesting that vimentin-deficiency has a larger effect during the response to IAV-infection than in
285 steady-state (**Supplemental Figure 3e**).
286
287 These results support an altered function of *Vim*$^{-/-}$ MoAMs in response to IAV that favors the
288 maintenance of Infiltrating phase genes and the suppression of Early Inflammatory phase genes to
289 confer protection from influenza-induced lung injury. Of note, these data demonstrate that the
290 greatest difference between genotypes occurs on day 3 p.i. and this represents the key timepoint
291 for the protective phenotype in *Vim*$^{-/-}$ mice.
292
293 ***Vim*$^{-/-}$ MoAMs fail to activate core pro-inflammatory genes in the early response to IAV**
294 Thus far, our results suggest that the maintenance of Infiltrating phase gene expression and
295 suppression of pro-inflammatory genes in *Vim*$^{-/-}$ MoAMs, particularly in the Early Inflammatory
296 phase, is responsible for the resilient phenotype observed in *Vim*$^{-/-}$ mice infected with IAV (see
297 Figure 1). To identify macrophage-specific genes involved in the Early Inflammatory Phase, we
298 focused on the $M_{(LPS)}$ response associated with the increased expression on day 3 p.i. in WT mice.
299 In MoAMs from *Vim*$^{-/-}$ mice, fewer $M_{(LPS)}$ genes exhibited peak expression on day 3 p.i. (**Figure 4a**).
300 Moreover, $M_{(LPS)}$ genes were enriched among those genes exhibiting the greatest expression
301 decrease in *Vim*$^{-/-}$ MoAMs compared with WT during the course of IAV response (**Supplemental**
302 **Figure 3b)**. Of the $M_{(LPS)}$ genes most decreased on at least one day, we find that the majority failed
303 to intensify expression on day 3 p.i. in *Vim*$^{-/-}$ MoAM compared with WT MoAM (**Figure 4b-c,**
304 **Supplemental Figure 4a)**. This core set of pro-inflammatory genes includes interferon-stimulated
305 genes (ISGs), such as *Ifit1, Irgm1, and Rsad2*, genes associated with chemokine pathways,
306 including *Ccrl2* and *Cxcl2,* and genes associated with pathogen sensing, *Fcgr1, and Tlr2* (**Figure**
307 **4b-c).** Complementary to the decrease in $M_{(LPS)}$ gene expression, $M_{(IL\text{-}4)}$ genes, such as *Cd36*,
308 *Cd11c,* and *Cd83*, previously associated with the Infiltrating phase, exhibited higher expression on
309 all days post IAV infection in *Vim*$^{-/-}$ MoAMs compared with WT MoAMs (**Supplemental Figures 3b,**

310 **c, 4b).** Collectively, these data suggest *Vim*$^{-/-}$ MoAMs fail to activate core pro-inflammatory genes
311 associated with the Early Inflammatory phase in response to IAV.
312
313 Prior work has demonstrated that macrophage activation is largely defined by the activity of cell-
314 type-specific transcription factors (TF) that poise regulatory elements for activation by stimulus-
315 specific TFs [42-44]. To better characterize the impact on gene regulation observed in *Vim*$^{-/-}$
316 MoAMs, we searched for TF binding sites enriched in the promoters of vimentin-dependent genes
317 associated with the Early Inflammatory phase. First, we classified the 440 Early Inflammatory
318 genes into those "most changed" and "least changed" in *Vim*$^{-/-}$ MoAMs based on their fold-change
319 compared with WT MoAMs (**Figure 4d-e, Supplemental Figure 4c**). Next, we performed motif-
320 finding on each gene set using a known sequence motifs database (see Methods). We found that
321 TF families previously implicated in an inflammatory response, such as *Jun-AP1* and *Rela*, were
322 significantly enriched among the most changed but not the least changed genes (**Figure 4f**). Some
323 Irf family motifs were differentially enriched between the two gene sets, while others were shared
324 (**Figure 4f**). As supported by induction of gene expression in IAV and the decrease observed in
325 *Vim*$^{-/-}$, those associated with ISGs (*Irf1*/7/9) were more likely to be affected by vimentin-deficiency
326 (**Figure 4f**). At the same time, *Irf8*, which is more generally involved in macrophage function,
327 exhibited similar enrichment in both groups (**Supplemental Figure 4e**). Furthermore, the CEBP
328 motif was associated with the most changed genes in *Vim*$^{-/-}$ MoAMs, and *Cebpb* was expressed
329 highly at both baseline and throughout IAV infection (**Figure 4f**). This observation is consistent with
330 *Cebpb*, a known macrophage TF that can also act in combination with AP1 factors (**Figure 4f),**
331 specifying poised regulatory elements in macrophages that activate genes on stimulation[45, 46].
332 On the other hand, ETS was the main TF family with motifs enriched in the least changed but not
333 the most changed genes (**Supplemental Figure 4d**). This family marginally includes PU.1, a well-
334 known myeloid lineage factor, but PU.1 is unlikely to have a specific role in IAV response
335 (**Supplemental Figure 4e**). Instead, the expression of *Elf1* and *Elf4* suggests that they may have

336 an interferon-independent antiviral role in influenza as previously reported [47], that is not impacted
337 by vimentin-deficiency. In summary, vimentin-deficiency impedes the stimulus-dependent
338 regulation of pro-inflammatory genes in MoAMs during the Early Inflammatory phase of IAV
339 infection. Although this effect leads to subtle changes in overall gene expression, it appears
340 sufficient to alter the MoAM function.
341
342 **Vimentin-deficient MoAMs are sufficient to confer protection from IAV-induced mortality**
343 We examined whether the loss of vimentin *in vitro* paralleled our *in vivo* observations of suppressed
344 pro-inflammatory gene expression (**Figure 3,4**). We polarized bone marrow-derived macrophages
345 (BMDMs) from WT and *Vim*$^{-/-}$ mice toward a pro-inflammatory (M1/$M_{(LPS)}$) phenotype or a reparative
346 (M2/ $M_{(IL-4)}$) phenotype through the administration of LPS or IL-4, respectively (**Figure 5a**). In line
347 with our *in vivo* observations, WT M1/$M_{(LPS)}$ macrophages had increased expression of pro-
348 inflammatory genes, such as *Tnf* and *Il1b*. The loss of vimentin suppressed the expression of M1
349 pro-inflammatory genes (**Figure 5b**) and increased the expression of M2/ $M_{(IL-4)}$ reparative genes
350 (*Mrc1, Arg1)* compared to WT macrophages (**Figure 5b**). Collectively, these data suggest that
351 vimentin plays a critical role in defining the macrophage pro-inflammatory phenotype.
352
353 To determine if vimentin plays a causal role in defining the pro-inflammatory function of recruited
354 MoAMs we used isochronic adoptive MoAM transfer experiments and molecular profiling in IAV-
355 infected mice. Bone marrow derived cells from WT or *Vim*$^{-/-}$ donor mice (CD45.2) were transferred
356 into irradiated WT recipient mice (CD45.1), allowing for the specific reconstitution of MoAMs with a
357 WT or *Vim*$^{-/-}$ genotype (**Figure 5c**). All mice showed reconstitution of donor hematopoietic cells in
358 peripheral blood above 85% (**Supplementary Figure 5a**). Following confirmed engraftment and
359 recovery, mice were infected with a lethal dose of IAV (**Figure 5c**). We found that IAV-infected WT
360 mice who received *Vim*$^{-/-}$ donor bone marrow exhibited significantly lower total protein concentration
361 in the BALF and lower wet-to-dry lung weight ratio than mice that received WT donor bone marrow,

362 indicating less severe alveolar damage (**Figure 5d-g**). Mice showed no difference in IAV replication
363 or clearance regardless of donor genotype (**Figure 5f**). Histopathological examination of IAV-
364 infected WT mice who received *Vim*$^{-/-}$ donor bone marrow demonstrated less severe alveolar
365 damage than those who received WT bone marrow (**Figure 5g**). As in *Vim*$^{-/-}$ mice (**Figure 1**), WT
366 mice with *Vim*$^{-/-}$ MoAMs exhibited lower levels of pro-inflammatory cytokines and chemokines
367 (**Figure 5h**). Taken together, these data support the notion that vimentin plays a causal role in
368 determining the pro-inflammatory function of recruited MoAM and drives IAV-induced lung injury.
369

370 **Discussion**

371 Monocytes are recruited to the lung during injury, where they differentiate into monocyte-derived
372 alveolar macrophages (MoAMs) in response to cues provided by the injured microenvironment. We
373 used a clinically relevant murine model of severe viral pneumonia to identify monocyte-derived
374 alveolar macrophage-specific gene expression patterns associated with three distinct phases of
375 IAV infection: Infiltrating, Early Inflammatory, and Late Inflammatory. WT MoAMs began expressing
376 pro-inflammatory genes and secreting tissue-damaging pro-inflammatory cytokines in the Early
377 Inflammatory phase, resulting in increased morbidity and mortality in influenza-infected wild-type
378 mice. Conversely, upon entering the IAV-infected alveolar microenvironment, *Vim*$^{-/-}$ MoAMs failed
379 to upregulate pro-inflammatory genes and suppressed the secretion of pro-inflammatory cytokines
380 conferring protection to the host. By leveraging the *Vim*$^{-/-}$ mouse's protective phenotype, we
381 investigated the transcriptional response following IAV infection and identified a core set of pro-
382 inflammatory genes that drive lung injury and mortality. Although prior studies have examined
383 macrophage gene expression at steady-state or single time points following IAV infection [48, 49],
384 by analyzing gene expression over a time course post-IAV infection, our results identified critical
385 temporal dynamics that shape the function of recruited monocyte-derived alveolar macrophages in
386 response to respiratory infections.

387

388 During IAV-infection, infected cells, and cells dying from necroptosis or pyroptosis, release PAMPs
389 and DAMPs, which activate signaling pathways to recruit additional effector cells, including MoAMs.
390 We reason that as monocytes extravasate and infiltrate the lung parenchyma, the differentiation of
391 WT MoAMs toward a pro-inflammatory phenotype involves activation of specific transcriptional
392 programs in response to the IAV-infected lung microenvironment. Understanding how MoAMs
393 communicate with resident cell populations to drive persistent inflammation (e.g., WT MoAMs) or
394 promote reparative processes (e.g., *Vim*$^{-/-}$ MoAMs) represents an active area of investigation.
395 During homeostasis, alveolar epithelial cells interact with tissue-resident macrophages via

396 receptor/ligand pairs CD200/CD200R, signal regulatory protein-α (SIRPα)/CD47, and CSF2R/GM-
397 CSF and immune/epithelial E-cadherin interactions [50, 51]. It follows that similar interactions occur
398 between alveolar epithelial cells and recruited MoAMs in the infected lung. These interactions, or
399 the disruption of these interactions, may activate specific transcriptional programs contributing to
400 the pro-inflammatory phenotype we observed in WT MoAMs. Investigating receptor/ligand
401 interactions and the secretion of molecules is limited by their short half-life and the requirement for
402 mass spectroscopy for their detection. Importantly, little information is known about specific
403 receptor/ligand interactions in recruited MoAMs during lung injury. We demonstrated that WT and
404 *Vim*$^{-/-}$ MoAMs encountered similar environmental signals associated with IAV infection (e.g.,
405 equivalent viral load, similar immune cell recruitment – see Figure 1). Notably, *Vim*$^{-/-}$ MoAMs
406 suppress pro-inflammatory genes and cytokines and maintain an increased expression of
407 reparative $M_{(IL\text{-}4)}$ genes throughout IAV infection. We hypothesize that the protective phenotype
408 displayed by recruited *Vim*$^{-/-}$ MoAMs may be the result of disrupted or altered receptor/ligand
409 interactions in the IAV-infected lung microenvironment. It will be important to investigate how the
410 temporal transcriptional changes observed in our study impact the ability of recruited MoAMs to
411 interact with and respond to other cell types in the lung microenvironment.
412
413 *In vitro* studies have established vimentin's role in essential cellular processes, such as cell motility,
414 cell signaling, and protein complex scaffolding [52-55]. Retinoic acid-inducible gene I, a cytosolic
415 PRR that detects viral RNA and mediates type I interferon expression, leads to increased vimentin
416 expression[56]. Our data support this previous observation, as type, I interferon genes peaked on
417 day 2 p.i., preceding the increase in vimentin gene expression in WT MoAMs. We confirmed
418 previous reports that *vimentin-deficient* mice fail to secrete mature IL-1b as assembly and activation
419 of the NLRP3 inflammasome requires vimentin [18, 19]. Complementary to our findings, vimentin's
420 interaction with NOD2, a cytoplasmic PRR, activated NF-κB and induced a pro-inflammatory
421 immune response in an inflammatory bowel disease model [20]. Of note, the suppressed pro-

422 inflammatory response observed in *Vim*$^{-/-}$ MoAMs does not appear to result from differing
423 macrophage maturation. In fact, genes involved in the transition from monocyte to macrophage-
424 like state, such as *Mafb*, were not differentially expressed between genotypes. Collectively, this
425 suggests that vimentin mediates the innate immune response(s) by regulating the expression of
426 pro-inflammatory genes.
427
428 Our findings demonstrate that depleting vimentin in MoAMs modulates the pro-inflammatory
429 response and protects the host, providing a rationale that vimentin could serve as a potential
430 therapeutic target during viral infection. Our group and others have shown that vimentin can be
431 therapeutically targeted in non-small cell lung cancer and other diseases such as idiopathic
432 pulmonary fibrosis [57, 58]. Molecules such as withaferin A, FiVe1, and simvastatin were used to
433 perturb the expression and/or assembly of vimentin filaments and led to the downregulation of
434 vimentin was accompanied by decreased cancer progression, decreased fibrosis and intermediate
435 filament disorganization, and cell death [58-61]. Collectively, these and our studies serve as a proof-
436 of-principle to support the development of pharmacological agents to target vimentin selectively.
437 These tools may be clinically beneficial in modulating the hyperinflammatory microenvironment of
438 the virus-infected lung.
439
440 Our study has several limitations. We used a well-established bone-marrow chimera mouse model
441 to demonstrate that *Vim*$^{-/-}$ MoAMs failed to upregulate pro-inflammatory genes and secrete pro-
442 inflammatory cytokines, which was sufficient to confer protection from IAV-induced lung injury and
443 mortality. Additionally, we showed that *Vim*$^{-/-}$ BMDMs expressed higher levels of M2/$M_{(IL\text{-}4)}$ markers
444 and lower levels of M1/$M_{(LPS)}$ markers, which appears to reflect the macrophage plasticity we
445 observed in our murine model of viral pneumonia. We caution the reader that while the framework
446 of M1/M2 polarization has provided a useful system to study macrophages in vitro, it is unlikely that
447 this occurs in tissue. This was shown by Xue *et al*., who found that the M1/M2 paradigm failed to

448 describe the transcriptome of human monocyte-derived and alveolar macrophages stimulated with
449 LPS/IFN-γ or IL-4/IL-13 in the presence of factors that recapitulate different tissue or disease
450 microenvironments [62]. Future studies could be improved by using a lineage mark to track the
451 recruitment and phenotype changes associated with recruited MoAMs *in vivo*. By generating a
452 *Vim*$^{fl/fl}$*Cx3cr1*^{CreERT2}*zsGreen* transgenic mouse, we could selectively delete vimentin and track the
453 recruitment of *GFP*$^{+}$*Vim*$^{-/-}$ alveolar macrophages during IAV infection. Regrettably, the vimentin-
454 floxed mouse is not yet available. Second, our RNA-seq data identified distinct transcriptional
455 phases of the IAV response in MoAMs; however, it is unclear whether different MoAM
456 subpopulations enter the lung at different time points from a single compartment. For example,
457 MoAMs may differentiate directly from circulating monocytes that extravasate from the pulmonary
458 capillaries into the alveolar space. Alternatively, MoAMs may stem from interstitial macrophages
459 already residing in the lung at steady-state. Using a *Vim*$^{fl/fl}$*Cx3cr1*^{CreERT2}*zsGreen* mouse, pulsed
460 lineage tracing would address these important questions.
461
462 In summary, our results define the temporal, transcriptional dynamics in recruited alveolar
463 macrophages that shape the response to respiratory infection and demonstrate that vimentin plays
464 an essential role in modifying macrophage phenotype and function. Moreover, we defined a core
465 set of pro-inflammatory genes whose upregulation during the early response to IAV drives lung
466 injury and mortality in wild-type, but not *Vim*$^{-/-}$ mice. We show that vimentin-deficient recruited
467 alveolar macrophages exhibit a dampened inflammatory response in a cell-autonomous manner,
468 sufficient to confer protection from IAV-induced mortality. Our data demonstrate that vimentin plays
469 a causal role in shaping the pro-inflammatory response in recruited MoAMs, promoting virus-
470 induced lung injury following IAV infection.
471

472 **Materials & Methods**

473 ***In silico single-cell RNA-seq data analysis.*** We queried a single-cell RNA-seq transcriptomic
474 data set derived from bronchoalveolar lavage samples from 10 patients with severe SARS-CoV-2
475 viral pneumonia[1]. We downloaded normalized counts tables and visualized the pre-determined
476 cell population clusters using Scanpy [63]. 40,000 single cells representing the four monocyte-
477 derived alveolar macrophages (MoAMs) populations were visualized as a UMAP. Mean expression
478 data of individual genes per cell population cluster were visualized as dot plots in Scanpy.

479 ***Mice.*** All experiments were performed using wild-type 129S or vimentin-null (*Vim*$^{-/-}$) 129S/V mice,
480 age 8-12 weeks. Wild-type mice were purchased from Taconic, *Vim*$^{-/-}$ mice were a gift from Albee
481 Messing (University of Wisconsin, Madison, WI). All animals were kept under pathogen-free
482 conditions, and all experiments were approved in accordance with Northwestern University's
483 Institutional Animal Care and Use Committee (IACUC) guidelines.

484 ***Bone marrow chimeras***. 8-12 week old recipient mice (Ptprc^{a}/Pep-Boy, CD45.1) were lethally
485 irradiated with a single dose of 1,000 cGy γ-radiation using a Cs-137–based Gammacell-40
486 irradiator (Nordion). Within 24 hours, fresh bone marrow cells (2 x 10^{6}) from either WT donor mice
487 or *Vim*$^{-/-}$ donor mice (CD45.2) were injected via retro-orbital injection. Mice were housed together
488 in individually ventilated cages and were given *ad libitum* access to food and water supplemented
489 with Trimetoprim/Sulfamethoxazole (TMP/SMX 40/8 mg formula, Hi-Tech Pharmacal) for 4 weeks
490 and then switched to standard housing regimen. Reconstituted mice were used for influenza
491 infection experiments ~4 weeks after transplantation. Engraftment was assessed after two weeks,
492 using flow cytometry to measure the percentage of CD45.1+ and CD45.2+ cells in peripheral blood
493 collected from the facial vein. All mice used for experiments showed reconstitution of the donor
494 (CD45.2) circulating leukocytes in peripheral blood above 85%.

495

496 ***Bone marrow derived macrophage (BMDM) polarization and RT-PCR.*** BMDMs were isolated
497 from wild-type 129S or vimentin-null (*Vim*$^{-/-}$) 129S/V mice, age 8-12 weeks, and treated with 100

498 ng/mL LPS or 20 ng/mL IL-4 to induce $M_{(LPS)}$ and $M_{(IL-4)}$ polarization, respectively. Cells were lysed
499 after 24 hours and RNA was extracted using RNeasy Mini kit (Qiagen) according to manufacturer's
500 protocol. RNA concentration was assessed using a NanoDrop platform (Thermo Fisher). RT-PCR
501 was run to assess gene expression changes (BioRad CFX).

502 ***Virus.*** H1N1 Influenza virus strain A/WSN/1933 (WSN) was propagated in fertile chicken eggs
503 (Sunnyside Hatchery) as previously described[4, 5]. Viral titers were determined by measuring
504 plaque-forming units (pfu) in Madin-Darby canine kidney epithelial cells (ATCC).

505 ***Plaque Assay.*** Confluent monolayers of Madin-Darby canine kidney epithelial cells were infected
506 with stock WSN virus in 1% BSA DMEM for 2h at 37°C. Plates were washed with PBS and an
507 overlay of 50% 2x replacement media (2x DMEM, 0.12M $NaHCO_3$, 2% penicillin-streptomycin, and
508 1% HEPES), 50% Avicel (2.35%), and N-acetyl trypsin (1.5μg/mL) remained on the cells for 72h at
509 37°C. Plates were washed with PBS and fixed with 0.2% PFA before staining the monolayers with
510 naphthalene blue-black stain.

511 ***In vivo influenza virus infection.*** 8-12 week old WT and *Vim*$^{-/-}$ 129S/V male mice were
512 anesthetized using isoflurane and intratracheally (i.t.) infected with 200 pfu WSN. Mice were
513 monitored daily, and weight was recorded every 24 hours.

514 ***Histology.*** Mice were euthanized, after which a 20-gauge angiocath was sutured into the trachea.
515 Heart and lungs were removed *en bloc*, and lungs were inflated with 0.8mL of 4% paraformaldehyde
516 (PFA) at a pressure not exceeding 16 cm H_2O. Tissue was fixed and embedded in paraffin. 5 μm
517 sections were stained with H&E by the Mouse Histology Phenotyping Laboratory (Northwestern
518 University, Chicago, IL). Tissue sections were visualized using TissueGnostics, a Tissue/Cell High
519 Throughput Imaging Analysis Systems (Vienna, Austria) and captured using TissueFAXS software
520 (TissueGnostics, Los Angeles, CA) at the Northwestern University Cell Imaging Facility
521 (Northwestern University, Chicago, IL).

522 ***Bronchoalveolar Lavage.*** A 20-gauge angiocath was ligated into the trachea, and 1mL of sterile
523 PBS was instilled into the lungs, then removed through the angiocath. This process was repeated
524 three times. Bronchoalveolar lavage fluid (BALF) was centrifuged at 500 x *g* for 10 min Protein
525 levels in the supernatant were measured by Bradford assay (Bio-Rad), and cytokine levels were
526 measured using a custom multiplex ELISA (ThermoFisher Scientific).
527 ***Wet-to-dry weight ratio.*** Mice were euthanized, and lungs were surgically removed *en bloc*. The
528 left lung was ligated, excised, and weighed in a tared container. The left lung was dried at 70°C in
529 a Speed-Vac SC100 evaporator (Thermo Scientific, Waltham, MA) until a constant weight was
530 obtained, and the wet-to-dry weight ratio was calculated.
531 ***Flow cytometry analysis of lung cell populations*****.** Mice were euthanized, and lungs were
532 perfused with 10mL HBSS with Ca^{2+} and Mg^{2+}. Lung loves were removed and inflated with enzyme
533 solution (5mL of 0.2 mg/mL DNase I and 2 mg/mL collagenase D in HBSS with Ca^{2+} and Mg^{2+})
534 using a 30-gauge needle. According to the manufacturer's instructions, tissue was minced and
535 processed in gentleMACS dissociator tubes (Miltenyi Biotec). Processed lungs were passed
536 through a 40μm cell strained, and RBCs were lysed using BD PharmLyse (BD Biosciences, San
537 Jose, CA). The remaining cells were counted using a Countess cell counter (Invitrogen, Grand
538 Island, NY). CD45 microbeads were added, and cells were eluted according to the Miltenyi
539 manufacturer's instructions. Cells were stained with viability dye Aqua (Invitrogen), and non-specific
540 antibody (Ab) binding was inhibited by adding Fc Block (553142, clone 2.4G2; BD Pharmingen).
541 Blocked cells were stained with a mixture of fluorochrome-conjugated Abs (see **Online**
542 **Supplemental Table 1** for list of Abs). Data were acquired on a BD LSR II flow cytometer using BD
543 FACSDiva software (BD Biosciences), and data analyses were performed using FlowJo software
544 (Tree Star, Ashland, OR). Cell populations were identified using a sequential gating strategy
545 (**Supplemental Figure 1b)**. Cell number was normalized to body weight.

546 ***Macrophage harvesting and flow sort.*** Mice were euthanized and perfused with 5 mL sterile PBS
547 by cardiac perfusion through the right ventricle. A 20-gauge angiocath was ligated into the trachea,
548 and the lung and trachea were removed *en bloc*. Lungs were instilled with 1 mL dispase (Corning)
549 through the angiocath, and a second suture was tied around the trachea to avoid leakage. Lungs
550 were placed in 50 mL tubes (Falcon) containing 750 μL cold dispase and rocked for 45 min at RT.
551 Trachea and angiocath were removed, and lungs were minced using curved-edge scissors.
552 Digested tissue was poured into 50 mL tubes containing 7 mL DMEM (Corning) and 14 μL DNase
553 I (50 mg/mL, Sigma). Tubes were rocked for 10 minutes at RT. Using serological pipettes, tissue
554 was gently further disrupted and subsequently filtered through 70 μm cell strainers and 40 μm
555 strainers (Corning). Tubes were rinsed with DMEM + 5% FBS and filtered through the same
556 strainers. Cell suspensions were centrifuged for 10 min at 1300 rpm, 4°C and pellets were
557 resuspended in 350 μL MACS buffer (Milteny). 100 μL CD11c magnetic microbeads (Milteny) were
558 added, and cells were eluted according to the Miltenyi manufacturer's instructions. Cells were
559 stained for CD11b (Biolegend), Siglec F (BD), Ly6C (eBioscience), CD45 (eBioscience), MHCII
560 (Biolegend), CD64 (Biolegend), Ly6G (BD), and NK1.1(BD). Viability dye (eFluor506, eBioscience)
561 was used to sort living cells only (**Online Supplemental Table 1**). Using sequential gating
562 (**Supplemental Figure 2b),** recruited alveolar macrophages (MoAMs) and tissue-resident alveolar
563 macrophages (TRAMs) were flow-sorted using a BD FACSaria III 5-laser cell sorter and 100 μm
564 nozzle (BD Biosciences). Of note, MoAMs were collected in the same gate as interstitial
565 macrophages (Ly6C-, CD64+); however, by 2 days p.i., interstitial macrophages were no longer
566 present in this gate (see **Online Supplemental Figure 2**). Flow-sorted cells were collected into 1.5
567 mL Eppendorf tubes containing 200 μL MACS buffer and centrifuged at 5,000 rpm for 5 min at RT.
568 Pellets were resuspended and lysed in RLT lysis buffer (Qiagen) and stored at -80°C until all time
569 points were collected.

570 ***RNA sequencing (RNA-seq).*** Samples collected from infected mice that at flow sort appeared
571 uninfected (had no infiltrating MoAM) were excluded from RNA isolation. RNA was isolated in all
572 samples at the same time to minimize the batch effect. All libraries for a given cell type were
573 prepared as a single batch for sequencing. Total RNA was isolated using RNeasy Plus Mini kits
574 (Qiagen). RNA quality (RIN) and quantity were assessed using a TapeStation 4200 (Agilent
575 Technologies). RIN scores ranged from 7.2 to 9.4, with an average of 8.6. Using poly(A) mRNA
576 magnetic enrichment kits from NEBNext (New England Biolabs), mRNA was isolated. cDNA
577 libraries were prepared using NEBNext Ultra DNA library kits (New England BioLabs) for Illumina.
578 Libraries were sequenced using high-output 75-cycle single-end kits on an Illumina NextSeq 500
579 sequencer to an average depth of 4.1 million reads per sample. Reads were demultiplexed
580 (bcl2fastq), trimmed, and aligned to reference genome mm10 using TopHat2[64]. Aligned reads
581 were mapped to genes using HTSeq with an Ensembl annotation (version 78)[65].
582 ***RNA-seq analysis.*** For k-means clustering, we used gene counts normalized to FPKM (Fragments
583 per Kilobase of transcript per Million mapped reads). Low counts were removed, with a cut-off set
584 as row sum >27 (# of samples used for analysis), yielding a gene counts table of 9,169 expressed
585 genes. One-way ANOVA with Benjamini-Hochberg (BH) FDR correction was used to define
586 differentially expressed genes over time. Genes with an FDR <0.05 were considered differentially
587 expressed, resulting in 2,623 DEGs. Clustering was performed on the 2,623 DEGs using k-means
588 clustering (GENE-E, https://software.broadinstitute.org/GENE-E/index.html).
589 For pairwise comparison, low counts were trimmed if CPM <2 in all replicates in the smallest group
590 of the comparison. EdgeR was used to define pairwise differentially expressed genes between WT
591 and *Vim*$^{-/-}$ MoAMs[66, 67]. Principal Component analysis (PCA) plots were generated using *pca*
592 function in R. Pearson correlation matrix, and heatmaps were generated using GENE-E. Gene
593 ontology (GO) analysis was run using Gorilla[68, 69]. Expressed genes, filtered for low counts
594 (9,169) were used as background. Gene set enrichment analysis (GSEA) was run using the
595 weighted pre-ranked setting based on the $\log_2$FC reported by edgeR [70, 71]. Gene sets associated

596 with specific processes were downloaded from KEGG (Cell Cycle) or Hallmark pathways
597 (Glycolysis, Oxidative Phosphorylation, IFN alpha (Type I interferon), IFNγ (Type II Interferon)
598 except for the custom gene sets described below. The 85 overlapping genes between the IFNα
599 and IFNγ Hallmark pathways were excluded from the IFNγ gene set. Overlaps between gene lists
600 were visualized using Venny (https://bioinfogp.cnb.csic.es/tools/venny/index.html).

601 ***Custom gene set generation.*** Custom gene sets for LPS/IFNγ and IL-4 stimulated were generated
602 by querying primary published data available in relevant experimental models. The final curated
603 gene sets, $M_{(LPS/IFN\gamma)}$ and $M_{(IL\text{-}4)}$, were derived from four primary publications [25, 39-41]. All four
604 publications used mouse bone-marrow-derived macrophages (BMDM) and stimulated them *in vitro*
605 with either LPS+IFNγor IL-4. Methodologies used included LC-ESI-MS/MS mass spectrometry,
606 microarray, and RNA-seq. A summary of the experimental approach, methods, and results for all
607 publications can be found in **Online Supplemental Table 2**. We included all genes that were
608 upregulated in at least one data set and could be converted into a unique Ensembl ID. Three genes
609 were found in both $M_{(LPS/IFN\gamma)}$ and $M_{(IL\text{-}4)}$ and were removed to avoid any overlap between gene sets.
610 These trimming steps resulted in two annotated gene sets of 110 LPS/IFNγ stimulated genes and
611 101 IL-4 stimulated genes (**Online Supplemental Table 2**).

612 ***Motif finding.*** We generated two gene sets of the 186 most and 254 least changed genes in *Vim*$^{-}$
613 $^{/-}$ MoAM by splitting the 440 genes of the Early Inflammatory cluster (Figure 2) based on whether
614 their $\log_2$(*Vim*$^{-/-}$/WT) expression on day 3 p.i. was above or below the mean of -0.23. (**Figure 6d,e)**.
615 To identify motifs that were enriched in either of these gene sets, we ran findmotifs.pl from the
616 HOMER package with default parameters and the mouse mm10 genome as background [45]. We
617 identified significantly enriched motifs as those with p-value < 0.05 in the known motif results.

618 ***Viral reads*****.** To identify viral reads within libraries, unmapped reads were aligned to the H1N1
619 reference genome. Reads for the H1N1 matrix protein 2 (M2), nucleoprotein (NP), and
620 neuraminidase (NA) were normalized by sample to the number of uniquely aligned (mm10) reads.

621 ***Statistics***. Analyses for cytokine levels, BALF protein, viral titer, and wet-to-dry ratio were
622 performed using GraphPad Prism (GraphPad Software). P values were calculated using a two-
623 tailed unpaired t-test assuming equal variance.
624

625 **Acknowledgments**

626 Histology services were provided by the Northwestern University Mouse Histology and Phenotyping
627 Laboratory, which is supported by NCI P30-CA060553 awarded to the Robert H Lurie
628 Comprehensive Cancer Center. Flow Cytometry was supported by the Northwestern University
629 RHLCCC Flow Cytometry Facility and a Cancer Center Support Grant (NCI CA060553). This
630 research was supported in part through the computational resources and staff contributions
631 provided by the Genomics Compute Cluster which is jointly supported by the Feinberg School of
632 Medicine, the Center for Genetic Medicine, and Feinberg's Department of Biochemistry and
633 Molecular Genetics, the Office of the Provost, the Office for Research, and Northwestern
634 Information Technology. The Genomics Compute Cluster is part of Quest, Northwestern
635 University's high performance computing facility, with the purpose to advance research in
636 genomics. Graphic design was created with BioRender.com. Kishore R. Anekalla was supported
637 by NIH T32 HL076139. Shang-Yang Chen was supported by a pre-doctoral AHA award
638 (19PRE34380200). Alexander V. Misharin was supported by N.I.H. grants U19AI135964,
639 P01AG049665, R01HL153312, and NUCATS COVID-19 Rapid Response Grant. Karen M. Ridge
640 was supported by N.I.H. grants P01AG049665 and P01GM096971. Bria M. Coates was supported
641 by funds provided by the Manne Research Institute COVID-19 Springboard Exploratory Research
642 Award and N.I.H. grant K08HL143127. Deborah R. Winter `was supported by the American Lung
643 Association, Arthritis National Research Foundation, American Thoracic Society, Scleroderma
644 Foundation, American Federation for Aging Research, American Heart Association
645 18CDA34110224, and NIH/NIAID U19AI135964. G.R.S.B. was supported by NIH grants

U19AI135964, P01AG049665, P01AG04966506S1, R01HL147575 and Veterans Affairs grant I01CX001777.

Author contributions: C.M.K., K.R.A., Y.H., B.M.C., A.V.M., D.R.W., K.M.R., contributed to the acquisition, analysis, and interpretation of the data and drafting the manuscript. M.C., G.G., S.C., M.T., Y.C., J.M.D., contributed to the acquisition and interpretation of data. C.M.K., K.R.A., Y.H., B.M.C., H.A.V., P.A.R., A.V.M., G.R.S.B., D.R.W., K.M.R. contributed to the conception and design of the study and interpretation of the data. All authors critically revised and approved the final version of the manuscript.

657 **References**
658

659 1. Grant, R.A., et al., *Circuits between infected macrophages and T cells in SARS-CoV-2*
660 *pneumonia.* 2021.
661 2. Matthay, M.A., et al., *Acute respiratory distress syndrome.* 2019. **5**(1): p. 18.
662 3. Calfee, C.S., et al., *Subphenotypes in acute respiratory distress syndrome: latent class*
663 *analysis of data from two randomised controlled trials.* Lancet Respir Med, 2014. **2**(8): p.
664 611-20.
665 4. Coates, B.M., et al., *Inflammatory Monocytes Drive Influenza A Virus-Mediated Lung Injury*
666 *in Juvenile Mice.* J Immunol, 2018. **200**(7): p. 2391-2404.
667 5. Misharin, A.V., et al., *Monocyte-derived alveolar macrophages drive lung fibrosis and*
668 *persist in the lung over the life span.* Journal of Experimental Medicine, 2017. **214**(8): p.
669 2387-2404.
670 6. Budinger, G.R.S., et al., *Distinctive features of severe SARS-CoV-2 pneumonia.* 2021.
671 **131**(14).
672 7. Yona, S., et al., *Fate Mapping Reveals Origins and Dynamics of Monocytes and Tissue*
673 *Macrophages under Homeostasis.* Immunity, 2013. **38**(1): p. 79-91.
674 8. Wang, Z., et al., *Early hypercytokinemia is associated with interferon-induced*
675 *transmembrane protein-3 dysfunction and predictive of fatal H7N9 infection.* 2014. **111**(2):
676 p. 769-74.
677 9. Yu, L., et al., *Clinical, virological, and histopathological manifestations of fatal human*
678 *infections by avian influenza A(H7N9) virus.* 2013. **57**(10): p. 1449-57.
679 10. Guo, J., et al., *The Serum Profile of Hypercytokinemia Factors Identified in H7N9-Infected*
680 *Patients can Predict Fatal Outcomes.* 2015. **5**: p. 10942.
681 11. Tate, M.D., et al., *Reassessing the role of the NLRP3 inflammasome during pathogenic*
682 *influenza A virus infection via temporal inhibition.* Sci Rep, 2016. **6**: p. 27912.
683 12. Coates, B.M., et al., *Inhibition of the NOD-Like Receptor Protein 3 Inflammasome Is*
684 *Protective in Juvenile Influenza A Virus Infection.* Front Immunol, 2017. **8**: p. 782.
685 13. Dawson, T.C., et al., *Contrasting effects of CCR5 and CCR2 deficiency in the pulmonary*
686 *inflammatory response to influenza A virus.* Am J Pathol, 2000. **156**(6): p. 1951-9.
687 14. Lin, K.L., et al., *CCR2-antagonist prophylaxis reduces pulmonary immune pathology and*
688 *markedly improves survival during influenza infection.* J Immunol, 2011. **186**(1): p. 508-15.
689 15. Gaurav, R., et al., *IL-33 Depletion in COVID-19 Lungs.* 2021. **160**(5): p. 1656-1659.
690 16. Nimmo, E.R., et al., *TLE1 modifies the effects of NOD2 in the pathogenesis of Crohn's*
691 *disease.* 2011. **141**(3): p. 972-981.e1-2.
692 17. Mor-Vaknin, N., et al., *Murine colitis is mediated by vimentin.* Sci Rep, 2013. **3**: p. 1045.
693 18. dos Santos, G., et al., *Vimentin regulates activation of the NLRP3 inflammasome.* Nat
694 Commun, 2015. **6**: p. 6574.
695 19. Lang, T., et al., *Macrophage migration inhibitory factor is required for NLRP3*
696 *inflammasome activation.* Nat Commun, 2018. **9**(1): p. 2223.
697 20. Stevens, C., et al., *The intermediate filament protein, vimentin, is a regulator of NOD2*
698 *activity.* Gut, 2013. **62**(5): p. 695-707.
699 21. Kamphuis, W., et al., *GFAP and vimentin deficiency alters gene expression in astrocytes*
700 *and microglia in wild-type mice and changes the transcriptional response of reactive glia in*
701 *mouse model for Alzheimer's disease.* Glia, 2015. **63**(6): p. 1036-56.
702 22. Abdulhasan, M., et al., *Stress Decreases Host Viral Resistance and Increases Covid*
703 *Susceptibility in Embryonic Stem Cells.* 2021. **17**(6): p. 2164-2177.
704 23. Bucher, H., et al., *Neutralization of both IL-1alpha/IL-1beta plays a major role in*
705 *suppressing combined cigarette smoke/virus-induced pulmonary inflammation in mice.*
706 Pulmonary Pharmacology & Therapeutics, 2017. **44**: p. 96-105.

24. Liu, M., et al., *C1q/TNF-related protein-9 promotes macrophage polarization and improves cardiac dysfunction after myocardial infarction.* 2019. **234**(10): p. 18731-18747.
25. Gensel, J.C., et al., *Predictive screening of M1 and M2 macrophages reveals the immunomodulatory effectiveness of post spinal cord injury azithromycin treatment.* Sci Rep, 2017. **7**: p. 40144.
26. Cai, B., et al., *MerTK signaling in macrophages promotes the synthesis of inflammation resolution mediators by suppressing CaMKII activity.* Sci Signal, 2018. **11**(549).
27. Xu-Vanpala, S., et al., *Functional heterogeneity of alveolar macrophage population based on expression of CXCL2.* Sci Immunol, 2020. **5**(50).
28. Herold, S., et al., *Influenza virus-induced lung injury: pathogenesis and implications for treatment.* Eur Respir J, 2015. **45**(5): p. 1463-78.
29. Imai, T., et al., *Identification and molecular characterization of fractalkine receptor CX3CR1, which mediates both leukocyte migration and adhesion.* Cell, 1997. **91**(4): p. 521-30.
30. Worthylake, R.A. and K. Burridge, *RhoA and ROCK promote migration by limiting membrane protrusions.* J Biol Chem, 2003. **278**(15): p. 13578-84.
31. Lammermann, T., et al., *Rapid leukocyte migration by integrin-independent flowing and squeezing.* Nature, 2008. **453**(7191): p. 51-5.
32. Starnes, T., et al., *The chemokine CXCL14 (BRAK) stimulates activated NK cell migration: implications for the downregulation of CXCL14 in malignancy.* Exp Hematol, 2006. **34**(8): p. 1101-5.
33. Watanabe, S., et al., *The role of macrophages in the resolution of inflammation.* 2019. **129**(7): p. 2619-2628.
34. Kratofil, R.M., P. Kubes, and J.F. Deniset, *Monocyte Conversion During Inflammation and Injury.* Arterioscler Thromb Vasc Biol, 2017. **37**(1): p. 35-42.
35. Sanchez, K.K., et al., *Cooperative Metabolic Adaptations in the Host Can Favor Asymptomatic Infection and Select for Attenuated Virulence in an Enteric Pathogen.* 2018. **175**(1): p. 146-158.e15.
36. Smallwood, H.S., et al., *Targeting Metabolic Reprogramming by Influenza Infection for Therapeutic Intervention.* Cell Reports, 2017. **19**(8): p. 1640-1653.
37. Singer, B.D. and N.S. Chandel, *Immunometabolism of pro-repair cells.* 2019. **129**(7): p. 2597-2607.
38. Ivashkiv, L.B., *IFNy: signalling, epigenetics and roles in immunity, metabolism, disease and cancer immunotherapy.* Nat Rev Immunol, 2018. **18**(9): p. 545-558.
39. Jablonski, K.A., et al., *Novel Markers to Delineate Murine M1 and M2 Macrophages.* PLoS One, 2015. **10**(12): p. e0145342.
40. Hans, C.P., et al., *Transcriptomics Analysis Reveals New Insights into the Roles of Notch1 Signaling on Macrophage Polarization.* 2019. **9**(1): p. 7999.
41. Becker, L., et al., *Unique proteomic signatures distinguish macrophages and dendritic cells.* PLoS ONE [Electronic Resource], 2012. **7**(3): p. e33297.
42. Gosselin, D., et al., *Environment drives selection and function of enhancers controlling tissue-specific macrophage identities.* Cell, 2014. **159**(6): p. 1327-40.
43. Ostuni, R., et al., *Latent enhancers activated by stimulation in differentiated cells.* Cell, 2013. **152**(1-2): p. 157-71.
44. Lavin, Y., et al., *Tissue-resident macrophage enhancer landscapes are shaped by the local microenvironment.* Cell, 2014. **159**(6): p. 1312-26.
45. Heinz, S., et al., *Simple combinations of lineage-determining transcription factors prime cis-regulatory elements required for macrophage and B cell identities.* 2010. **38**(4): p. 576-89.
46. Heinz, S., et al., *Effect of natural genetic variation on enhancer selection and function.* Nature, 2013. **503**(7477): p. 487-92.

758 47. Seifert, L.L., et al., *The ETS transcription factor ELF1 regulates a broadly antiviral program*
759 *distinct from the type I interferon response.* PLoS Pathog, 2019. **15**(11): p. e1007634.
760 48. Zhang, J., et al., *Two waves of pro-inflammatory factors are released during the influenza*
761 *A virus (IAV)-driven pulmonary immunopathogenesis.* 2020. **16**(2): p. e1008334.
762 49. Tate, M.D., et al., *Critical role of airway macrophages in modulating disease severity*
763 *during influenza virus infection of mice.* Journal of Virology, 2010. **84**(15): p. 7569-80.
764 50. Hussell, T. and T.J. Bell, *Alveolar macrophages: plasticity in a tissue-specific context.*
765 2014. **14**(2): p. 81-93.
766 51. Bissonnette, E.Y., et al., *Cross-Talk Between Alveolar Macrophages and Lung Epithelial*
767 *Cells is Essential to Maintain Lung Homeostasis.* 2020. **11**: p. 583042.
768 52. Li, Q.F., et al., *Critical role of vimentin phosphorylation at Ser-56 by p21-activated kinase*
769 *in vimentin cytoskeleton signaling.* J Biol Chem, 2006. **281**(45): p. 34716-24.
770 53. Ivaska, J., et al., *Novel functions of vimentin in cell adhesion, migration, and signaling.* Exp
771 Cell Res, 2007. **313**(10): p. 2050-62.
772 54. Mendez, M.G., S. Kojima, and R.D. Goldman, *Vimentin induces changes in cell shape,*
773 *motility, and adhesion during the epithelial to mesenchymal transition.* FASEB J, 2010.
774 **24**(6): p. 1838-51.
775 55. Yoon, M., et al., *Motile properties of vimentin intermediate filament networks in living cells.*
776 J Cell Biol, 1998. **143**(1): p. 147-57.
777 56. de Rivero Vaccari, J.P., et al., *Astrogliosis involves activation of retinoic acid-inducible*
778 *gene-like signaling in the innate immune response after spinal cord injury.* Glia, 2012.
779 **60**(3): p. 414-21.
780 57. Richardson, A.M., et al., *Vimentin Is Required for Lung Adenocarcinoma Metastasis via*
781 *Heterotypic Tumor Cell-Cancer-Associated Fibroblast Interactions during Collective*
782 *Invasion.* 2018. **24**(2): p. 420-432.
783 58. Berr, A.L., et al., *Vimentin is Required for Tumor Progression and Metastasis in a Mouse*
784 *Model of Non-Small Cell Lung Cancer.* bioRxiv, 2020: p. 2020.06.04.130963.
785 59. Bargagna-Mohan, P., et al., *Withaferin A effectively targets soluble vimentin in the*
786 *glaucoma filtration surgical model of fibrosis.* 2013. **8**(5): p. e63881.
787 60. Bollong, M.J., et al., *A vimentin binding small molecule leads to mitotic disruption in*
788 *mesenchymal cancers.* 2017. **114**(46): p. E9903-E9912.
789 61. Trogden, K.P., et al., *An image-based small-molecule screen identifies vimentin as a*
790 *pharmacologically relevant target of simvastatin in cancer cells.* 2018. **32**(5): p. 2841-2854.
791 62. Xue, J., et al., *Transcriptome-based network analysis reveals a spectrum model of human*
792 *macrophage activation.* 2014. **40**(2): p. 274-88.
793 63. Wolf, F.A., P. Angerer, and F.J. Theis, *SCANPY: large-scale single-cell gene expression*
794 *data analysis.* Genome Biol, 2018. **19**(1): p. 15.
795 64. Kim, D., et al., *TopHat2: accurate alignment of transcriptomes in the presence of*
796 *insertions, deletions and gene fusions.* 2013. **14**(4): p. R36.
797 65. Anders, S., P.T. Pyl, and W. Huber, *HTSeq--a Python framework to work with high-*
798 *throughput sequencing data.* Bioinformatics, 2015. **31**(2): p. 166-9.
799 66. Robinson, M.D., D.J. McCarthy, and G.K. Smyth, *edgeR: a Bioconductor package for*
800 *differential expression analysis of digital gene expression data.* Bioinformatics, 2010.
801 **26**(1): p. 139-40.
802 67. McCarthy, D.J., Y. Chen, and G.K. Smyth, *Differential expression analysis of multifactor*
803 *RNA-Seq experiments with respect to biological variation.* Nucleic Acids Res, 2012.
804 **40**(10): p. 4288-97.
805 68. Eden, E., et al., *Discovering motifs in ranked lists of DNA sequences.* PLoS Comput Biol,
806 2007. **3**(3): p. e39.
807 69. Eden, E., et al., *GOrilla: a tool for discovery and visualization of enriched GO terms in*
808 *ranked gene lists.* BMC Bioinformatics, 2009. **10**: p. 48.

809 70. Mootha, V.K., et al., *PGC-1alpha-responsive genes involved in oxidative phosphorylation*
810 *are coordinately downregulated in human diabetes.* 2003. **34**(3): p. 267-73.
811 71. Subramanian, A., et al., *Gene set enrichment analysis: a knowledge-based approach for*
812 *interpreting genome-wide expression profiles.* Proc Natl Acad Sci U S A, 2005. **102**(43): p.
813 15545-50.

814
815

Figure Legends

Figure 1. Vimentin-null mice are protected from influenza-induced lung injury and mortality. **a**) Uniform Manifold Approximation and Projection (UMAP) of 40,248 cells annotated as monocyte-derived alveolar macrophages (MoAMs) obtained from 10 patients with severe COVID-19 disease within 48 hours after intubation. **b)** Fraction of cells expressing *VIM* and mean expression in each MoAM cluster. **c)** Visualization of *IL1-B, CCL3, CXCL2, C1QA*, and *MERTK* expression in MoAM cells using density projection plots. Scale bar represents expression averaged within hexagonal areas on UMAP. **d)** Fraction of cells expressing the representative genes and their mean expression in each MoAM cluster. **e)** Survival of wild-type (WT) and *Vim*$^{-/-}$ mice intratracheally infected with a lethal dose of influenza A virus (IAV) (200pfu) was measured and compared. Survival curves were analyzed using log-rank test, p-value =0.001. Data shown are n=12 per group. **f**) Lung wet-to-dry ratio measured at day 3 and 5 p.i. (n = 8-11/timepoint) **g**) Bronchoalveolar lavage fluid (BALF) protein levels measured by Bradford assay, n=5/timepoint. In **f** and **g**, differences between genotypes on each day were assessed by t-test. p-values were 0.0015 and <0.0001, for 3 and 5 days p.i., respectively. **h)** Representative images of murine lung architecture at day 7 p.i. assessed by H&E staining, scale bar 100 um. **i**) Viral titer assessed by plaque assay. The difference between genotypes was statistically not significant. n=5-9/timepoint. **j**) Flow cytometric analysis of tissue-resident (TRAMs) and infiltrating monocyte-derived alveolar macrophages (MoAMs) out of the total lung CD45+ cell population normalized to body weight during the IAV response, n=4/timepoint. **k)** Levels of inflammatory cytokines in BALF were assessed using a custom multiplex ELISA. n=3-4/timepoint. Bar graphs represent mean, error bars represent SD, differences between genotypes on each day were assessed by t-test. * p<0.05

Supplemental Figure 1. **a**) UMAP of 77,146 cells annotated by cell type obtained from 10 patients with severe COVID-19 disease within 48 hours after intubation. **b)** Quantification of H1N1 viral RNA molecules detected among RNA isolated from MoAMs, normalized to the number of reads uniquely aligned to the mouse genome (mm10) for each sample. Bar graphs represent mean, error bars represent SD. **c)** Gating strategy used for flow cytometry analysis of neutrophils, TRAMs, interstitial macrophages (IM), and MoAMs. **d**) Flow cytometric analysis demonstrated no differences in the number of neutrophils out of the total lung CD45+ cell population normalized to body weight between *Vim*$^{-/-}$ and WT mice during the IAV response.

Figure 2. Wild-type monocyte-derived alveolar macrophages exhibit gene expression patterns associated with three phases of influenza A viral infection. a) Heatmap of normalized expression of 2,623 differentially expressed genes (ANOVA p-value <0.05). Z-score normalization for each row was applied to gene expression (FPKM) data. K-means clustering (k=3) identified three clusters: Infiltrating (1131 genes), Early Inflammatory (440 genes), Late Inflammatory (1052 genes). **b)** Mean z-scores calculated across genes for each cluster **c)** Gene Ontology (GO) term enrichment for each phase. **d)** Bar graphs of gene expression (FPKM) for representative genes in each phase. Error bars represent SD. (ANOVA p-value <0.05). **e)** Bubble plot representing the proportion of genes (%) within each process that had an expression above the row mean. Color gradient represents the mean z-score of expression across genes. **f)** Enrichment of gene sets in each cluster as defined in A. Asterisk represents significantly enriched overlaps (hypergeometric p-value <0.0018, FWER = 0.05). The dotted line indicates an expected enrichment score of 1. n=3-4 per group. Ox Phos = Oxidative phosphorylation.

Supplemental Figure 2. a) Schematic of experimental design and workflow. WT or *Vim*$^{-/-}$ mice were infected with a lethal dose of influenza A virus (200 pfu). MoAMs were sorted by flow cytometry (FACS) from lungs on 2, 3, 4, and 6 days p.i. Total RNA was isolated, mRNA was enriched, and bulk RNA-seq was performed. Principal component analysis (PCA) was used to visualize replicates.

867 **b)** Sequential gating strategy used for FACS collection of TRAMs and MoAMs **c)** Violin plots of
868 log_2(FPKM+1) counts data for all genes in each cluster. Solid lines represent median, dotted lines
869 represent quartiles. **d)** Bar graphs of gene expression (FPKM) in MoAMs for representative genes
870 in each phase. Error bars represent SD. (ANOVA p-value <0.05).
871
872
873 **Figure 3. *Vim*$^{-/-}$ MoAMs modulate expression of Infiltrating and Early Inflammatory, but not**
874 **Late Inflammatory phase genes. a)** Volcano plots of differentially expressed genes (edgeR p-
875 value<0.05, and edgeR reported log_2FC>|1.0|) between *Vim*$^{-/-}$ and WT MoAMs on each day post-
876 infection. The number of genes downregulated (blue) and upregulated (red) in *Vim*$^{-/-}$ compared to
877 WT MoAMs are shown. **b)** GO term enrichment across days p.i. in the downregulated (blue) and
878 upregulated (red) genes in *Vim*$^{-/-}$ compared to WT MoAMs. Scale represents -log_{10} p-value. **c-e)**
879 Line graphs on the left represent mean adapted z-scores, calculated across genes for each cluster
880 in WT MoAMs and *Vim*$^{-/-}$ MoAMs. Shading represents WT MoAMs inter-quartile range (IQR). Dot
881 plots to the right represent % of genes at each timepoint expressed above their WT mean. Each
882 dot represents a replicate. Lines represent the median **f)** % genes in each cluster that exhibit
883 decreased or increased expression in *Vim*$^{-/-}$ MoAMs compared to WT MoAMs (n=3-4 per group).
884 Decreased genes defined as log_2FC < -0.58 (FC of 1.5); increased genes defined as log_2FC>0.58.
885
886 **Supplemental Figure 3. a**) Principal component analysis (PCA) of *Vim*$^{-/-}$ MoAMs replicates. **b)**
887 Gene Set Enrichment Analysis (GSEA) enrichment plots. GSEA was performed on gene lists
888 ranked by edgeR reported fold-change between *Vim*$^{-/-}$ and WT MoAMs at each time point.
889 Normalized enrichment scores (NES) are shown. Asterisks indicate statistically significant adjusted
890 p-values <0.05. **c)** Scatter plot of z-score normalized gene expression across genes in $M_{(IL-4)}$ vs Cell
891 Cycle. Pearson correlation coefficients (r) across WT or *Vim*$^{-/-}$ MoAM replicates, and associated p-
892 values are shown. **d)** Heatmap matrix of Pearson correlation between processes, asterisk indicates
893 p-value <0.05. **e)** Violin plots representing the log_2FC between *Vim*$^{-/-}$ and WT in tissue-resident
894 alveolar macrophages (TRAMs) at steady-state (0 dpi) for each gene by biological cluster and
895 biological process. Solid lines represent median, dotted lines represent quartiles **f)** Heatmap
896 showing pairwise Pearson correlation of mean gene expression across replicates between each
897 time point in WT and *Vim*$^{-/-}$ MoAMs. Pearson correlation coefficient values are shown within each
898 square. Scale bar represents Pearson correlation coefficient. **g)** Heatmap of normalized expression
899 of 2,623 genes as defined in Figure 2a. *Vim*$^{-/-}$ data was normalized to the WT mean and standard
900 deviation (adapted z-score). **h)** Violin plots representing the log_2FC between *Vim*$^{-/-}$ and WT for each
901 gene by cluster in MoAMs. Solid lines represent median, dotted lines represent quartiles. Asterisks
902 indicate adjusted p-value <0.05
903
904
905 **Figure 4. Protective phenotype of *Vim*$^{-/-}$mice is associated with the failure of *Vim*$^{-/-}$MoAMs to**
906 **activate core pro-inflammatory genes in the early response to IAV. a)** Percent (%) $M_{(LPS)}$ genes
907 peaking in expression on each day post-infection in WT and *Vim*$^{-/-}$ MoAMs **b)** Bar graphs of gene
908 expression (FPKM) for representative $M_{(LPS)}$ genes present in the leading edge of at least 1 day
909 from GSEA. Error bars represent SD. **c)** Heatmap of normalized expression of 84 $M_{(LPS)}$ genes
910 present in the GSEA leading edge on at least 1 day (indicated by a color-coded bar on the left).
911 Adapted Z-score normalization using WT mean and standard deviation for each row were applied
912 to gene expression (FPKM) data. **d)** Histogram representing the distribution of log_2FC between *Vim*$^{-}$
913 $^{/-}$ and WT MoAMs on 3 dpi of the Early Inflammatory phase (440 genes). The dashed line represents
914 the mean of the distribution. The number of genes less than (186) and greater than (254) the mean
915 are shown. Genes with log_2FC between *Vim*$^{-/-}$ and WT MoAMs less than the mean represent those
916 genes that are most changed between *Vim*$^{-/-}$ and WT MoAMs. **e)** Mean adapted z-scores were
917 calculated across genes for most (186) and least (254) changed genes on 3 dpi in the Early

Inflammatory Phase in WT and *Vim*$^{-/-}$ MoAMs. **f)** HOMER known motif analysis using genomic background of most changed genes on 3 dpi in the Early Inflammatory Phase (186 genes). Motif logos are shown below motif names. -$\log_{10}$pvalues of enrichment in most or least changed gene set is shown. Log_2(FPKM+1) average gene expression of transcription factor family members are shown for WT TRAMs and WT IMs at steady-state (0 dpi) and 2-6 dpi for WT MoAMs. $\log_2$FC between *Vim*$^{-/-}$ and WT MoAM gene expression of transcription factor family members on each dpi. (n=3-4)

Supplemental Figure 4. a) Mean adapted z-scores for $M_{(LPS)}$ and $M_{(IL\text{-}4)}$ genes present in the leading edge of at least 1 day from GSEA in WT and *Vim*$^{-/-}$ MoAMs. **b)** Heatmap of normalized expression of $M_{(IL\text{-}4)}$ genes present in the leading edge of at least 1 day from GSEA. Adapted Z-score normalization for each row was applied to gene expression (FPKM) data. Bar graphs of gene expression (FPKM) for representative $M_{(IL\text{-}4)}$ genes present in the leading edge of at least 1 day from GSEA. Error bars represent SD. **c)** Heatmap of normalized expression of 186 most changed, and 254 least changed genes on 3dpi of the Early Inflammatory Phase. Adapted Z-score normalization for each row was applied to gene expression (FPKM) data. **d)** HOMER known motif analysis using genomic background of least changed genes on 3 dpi in the Early Inflammatory Phase (254 genes). Motif logos are shown below motif names. Log_2(FPKM+1) average gene expression of transcription factor family members is shown for WT TRAMs and WT IMs at steady-state (0 dpi) and 2-6 dpi for WT MoAMs. $\log_2$FC between *Vim*$^{-/-}$ and WT MoAM gene expression of transcription factor family members on each dpi. (n=3-4). **e)** Motif logos are shown below motif names. -$\log_{10}$pvalues of enrichment in most or least changed gene set is shown.

Figure 5. Vimentin-deficiency in the MoAM compartment is sufficient to protect from influenza A virus-induced lung damage and mortality. a) Schematic of experimental design. BMDM were isolated from either WT or Vim-/- mice. BMDM were treated with LPS or IL-4 to polarize macrophages towards an $M_{(LPS)}$ or $M_{(IL\text{-}4)}$ state, respectively. Gene expression was assessed by qPCR **b)** Expression of genes characterizing a pro-inflammatory and reparative macrophage state in WT and *Vim*$^{-/-}$ macrophages. n = 2, in duplicate. Bar graphs represent mean relative fold change, error bars represent SEM. Differences between genotypes were assessed by t-test. **c)** Schematic of the experimental design. Recipient mice (CD45.1) were irradiated and reconstituted with bone marrow cells from WT or *Vim*$^{-/-}$ donor mice (CD45.2). After a 30-day recovery period, chimeric mice were intratracheally (i.t.) infected with a lethal dose of IAV at 5 days p.i. and subjected to analyses. **d)** Bronchoalveolar lavage fluid (BALF) protein levels measured by Bradford assay, n=3-4 **e)** Lung wet-to-dry ratio measured at day 5 p.i. n=7-10. **f**) Viral titer assessed by plaque assay. n=11-14. **g)** Representative images of murine lung architecture at day 5 p.i. assessed by H&E staining, scale bar 100 um. **h)** Levels of inflammatory cytokines in BALF assessed using a custom multiplex ELISA. n=4-9. Bar graphs represent mean, error bars represent SEM. Differences between genotypes were assessed by t-test. * $p<0.05$.

Supplemental Figure 5. Representative flow cytometry dot plots demonstrate successful engraftment of WT and *Vim*$^{-/-}$ CD45.2 donor cells into CD45.1 recipient mice.

Figure 1

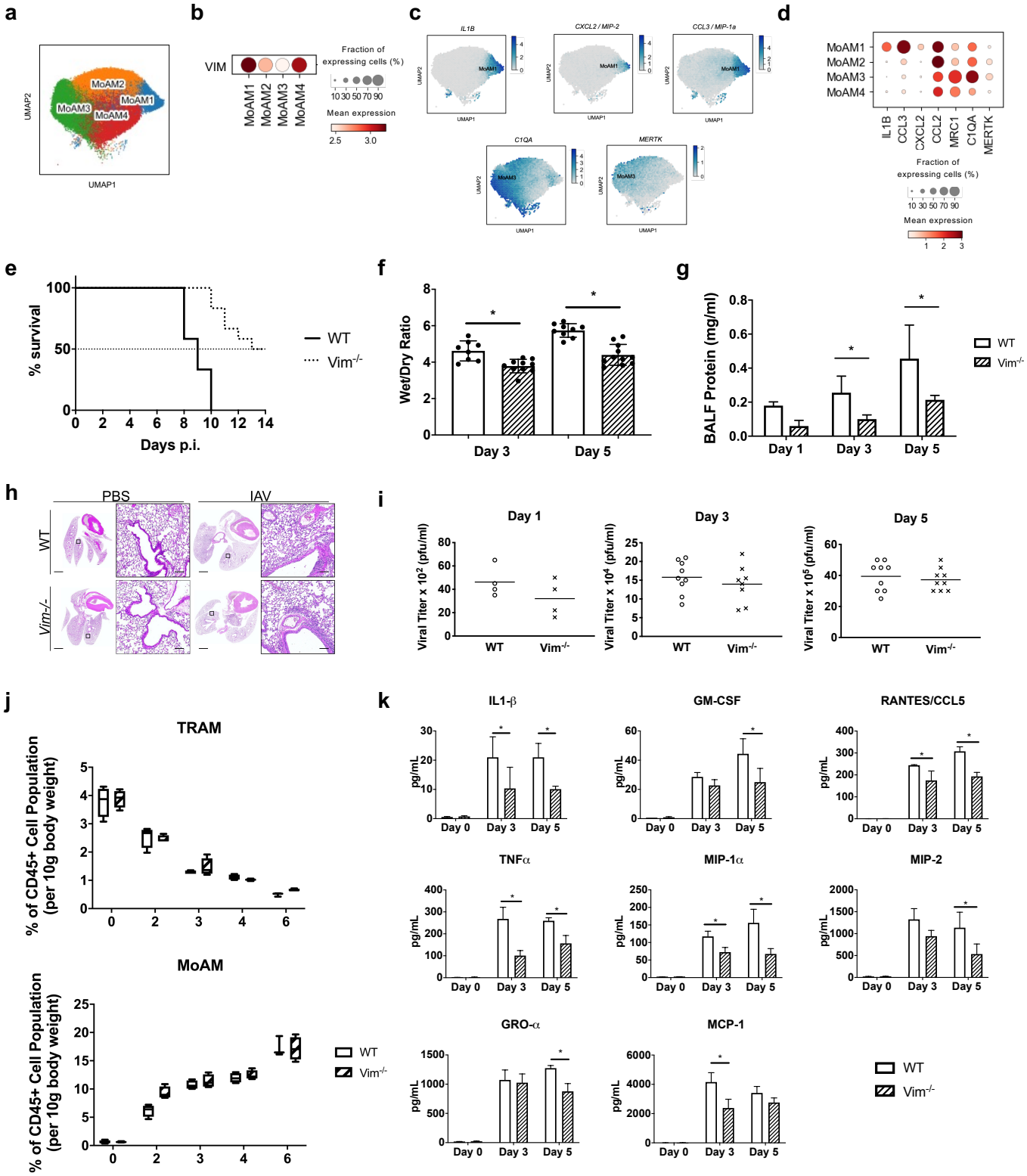
a
MoAM2
MoAM1
MoAM3
MoAM4
UMAP2
UMAP1
b
VIM
MoAM1
MoAM2
MoAM3
MoAM4
Fraction of expressing cells (%)
10 30 50 70 90
Mean expression
2.5 3.0
c
IL1B
CXCL2 / MIP-2
CCL3 / MIP-1a
C1QA
MERTK
d
MoAM1
MoAM2
MoAM3
MoAM4
IL1B
CCL3
CXCL2
CCL2
MRC1
C1QA
MERTK
Fraction of expressing cells (%)
10 30 50 70 90
Mean expression
1 2 3
e
% survival
Days p.i.
WT
Vim-/-
f
Wet/Dry Ratio
Day 3
Day 5
g
BALF Protein (mg/ml)
Day 1
Day 3
Day 5
WT
Vim-/-
h
PBS
IAV
WT
Vim-/-
i
Day 1
Day 3
Day 5
Viral Titer x 10^2 (pfu/ml)
Viral Titer x 10^4 (pfu/ml)
Viral Titer x 10^5 (pfu/ml)
WT
Vim-/-
j
TRAM
MoAM
% of CD45+ Cell Population (per 10g body weight)
WT
Vim-/-
k
IL1-β
GM-CSF
RANTES/CCL5
TNFα
MIP-1α
MIP-2
GRO-α
MCP-1
pg/mL
Day 0
Day 3
Day 5
WT
Vim-/-

Supplemental Figure 1

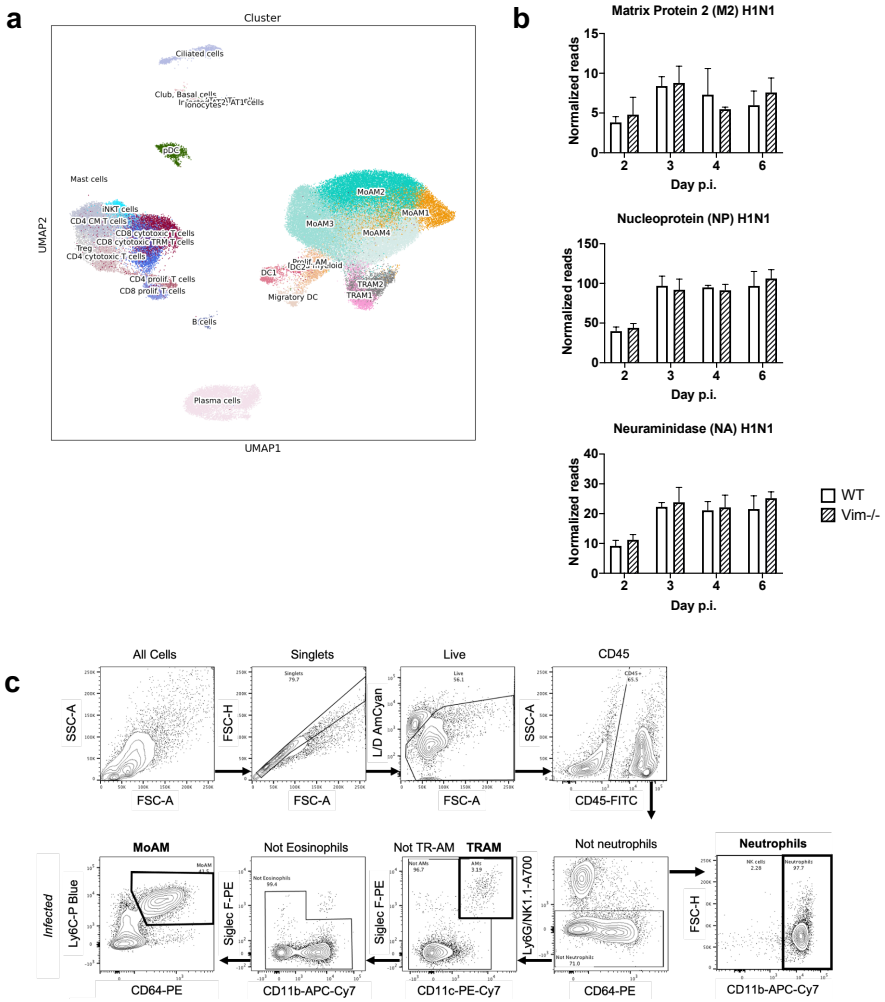

Figure 2

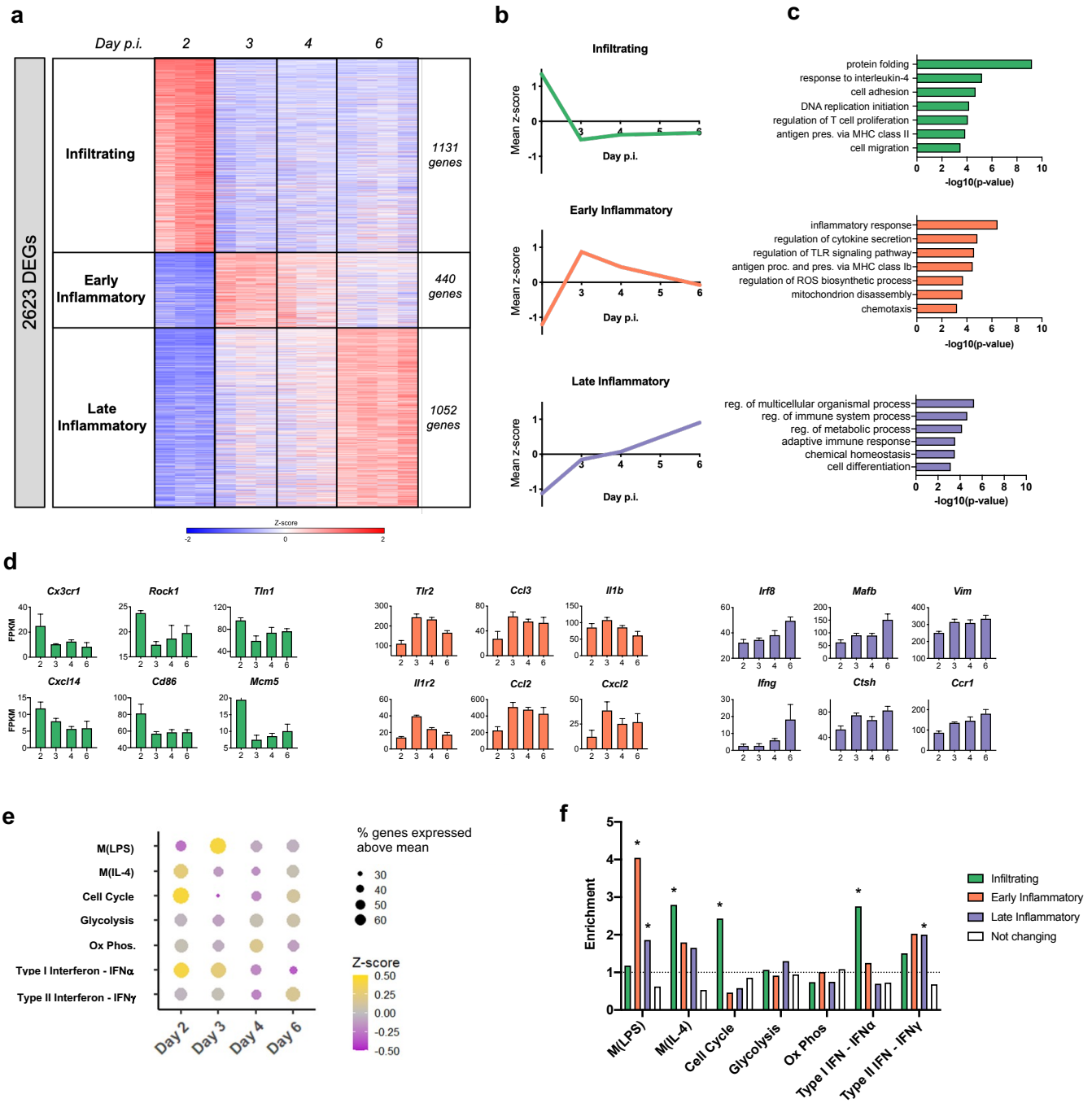
a
Day p.i.
2
3
4
6
2623 DEGs
Infiltrating
Early Inflammatory
Late Inflammatory
1131 genes
440 genes
1052 genes
Z-score
-2
0
2
b
Infiltrating
Early Inflammatory
Late Inflammatory
Mean z-score
Day p.i.
c
protein folding
response to interleukin-4
cell adhesion
DNA replication initiation
regulation of T cell proliferation
antigen pres. via MHC class II
cell migration
inflammatory response
regulation of cytokine secretion
regulation of TLR signaling pathway
antigen proc. and pres. via MHC class Ib
regulation of ROS biosynthetic process
mitochondrion disassembly
chemotaxis
reg. of multicellular organismal process
reg. of immune system process
reg. of metabolic process
adaptive immune response
chemical homeostasis
cell differentiation
-log10(p-value)
d
Cx3cr1
Rock1
Tln1
Tlr2
Ccl3
Il1b
Irf8
Mafb
Vim
Cxcl14
Cd86
Mcm5
Il1r2
Ccl2
Cxcl2
Ifng
Ctsh
Ccr1
FPKM
e
M(LPS)
M(IL-4)
Cell Cycle
Glycolysis
Ox Phos.
Type I Interferon - IFNα
Type II Interferon - IFNγ
Day 2
Day 3
Day 4
Day 6
% genes expressed above mean
30
40
50
60
Z-score
0.50
0.25
0.00
-0.25
-0.50
f
Enrichment
Infiltrating
Early Inflammatory
Late Inflammatory
Not changing
M(LPS)
M(IL-4)
Cell Cycle
Glycolysis
Ox Phos
Type I IFN - IFNα
Type II IFN - IFNγ

Supplemental Figure 2

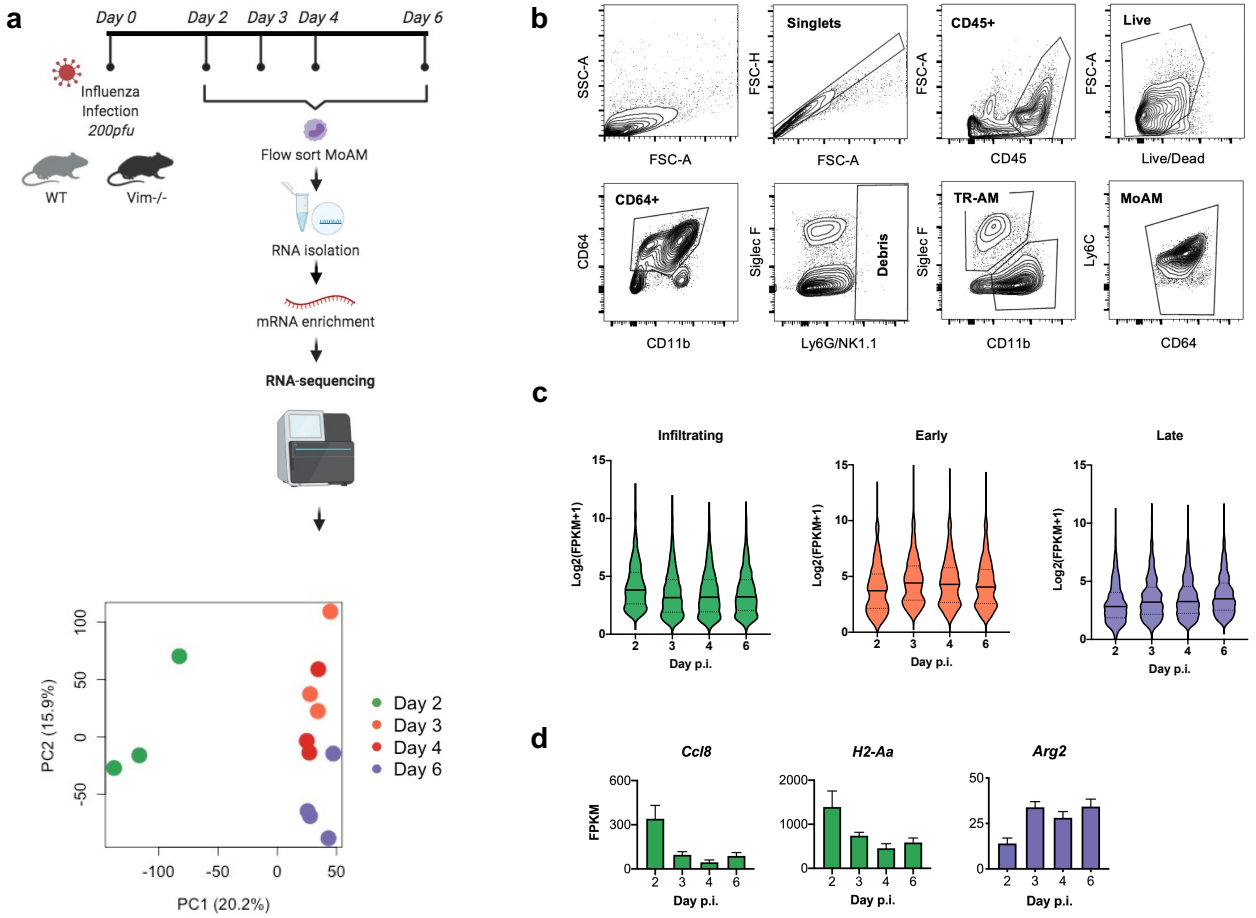

Figure 3

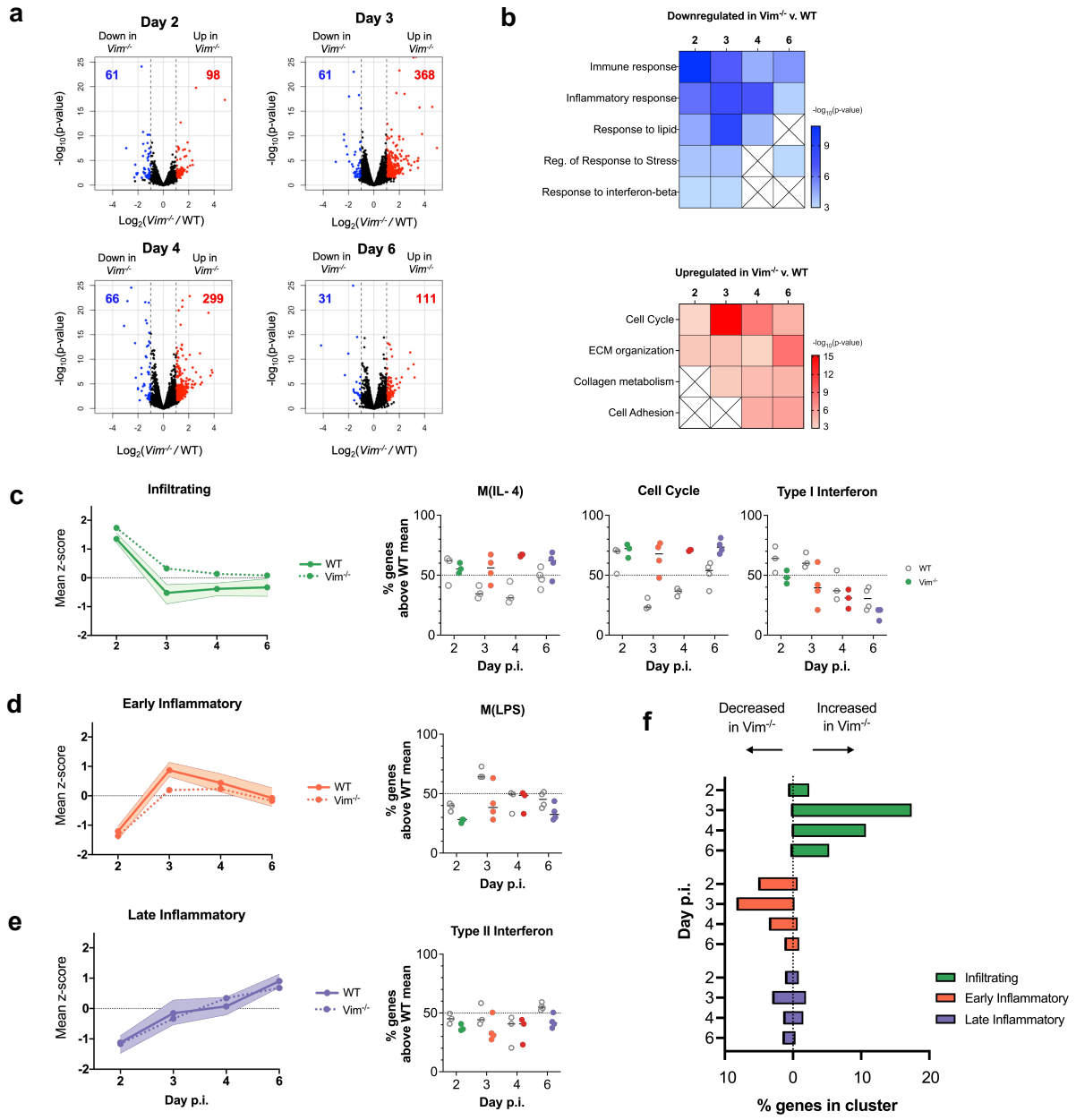
a
Day 2
Down in Vim-/-
Up in Vim-/-
61
98
Day 3
61
368
Day 4
66
299
Day 6
31
111
-log10(p-value)
Log2(Vim-/- / WT)
b
Downregulated in Vim-/- v. WT
Immune response
Inflammatory response
Response to lipid
Reg. of Response to Stress
Response to interferon-beta
-log10(p-value)
Upregulated in Vim-/- v. WT
Cell Cycle
ECM organization
Collagen metabolism
Cell Adhesion
c
Infiltrating
Mean z-score
WT
Vim-/-
M(IL- 4)
% genes above WT mean
Cell Cycle
Type I Interferon
Day p.i.
d
Early Inflammatory
M(LPS)
e
Late Inflammatory
Type II Interferon
f
Decreased in Vim-/-
Increased in Vim-/-
Day p.i.
Infiltrating
Early Inflammatory
Late Inflammatory
% genes in cluster

Supplemental Figure 3

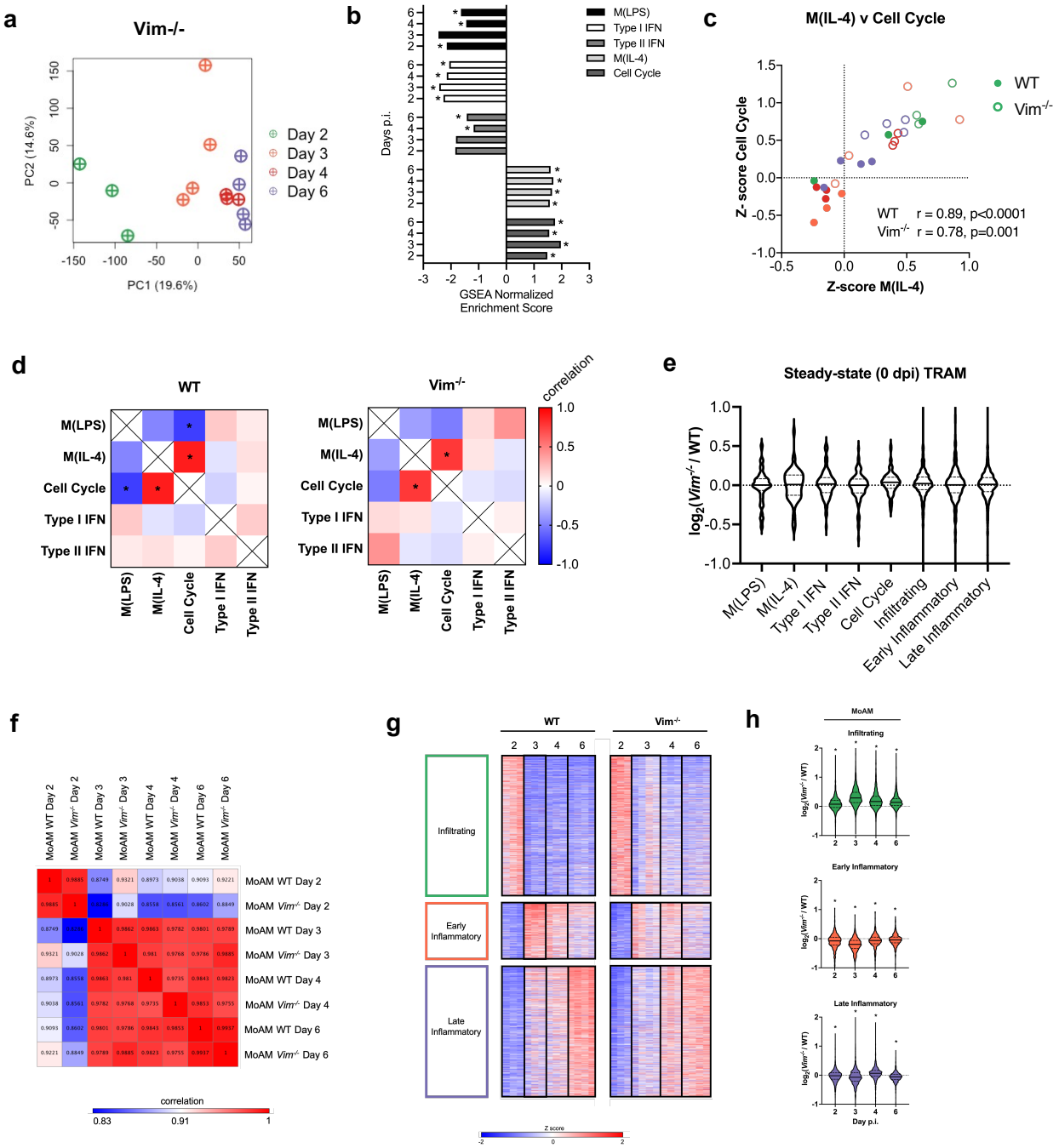

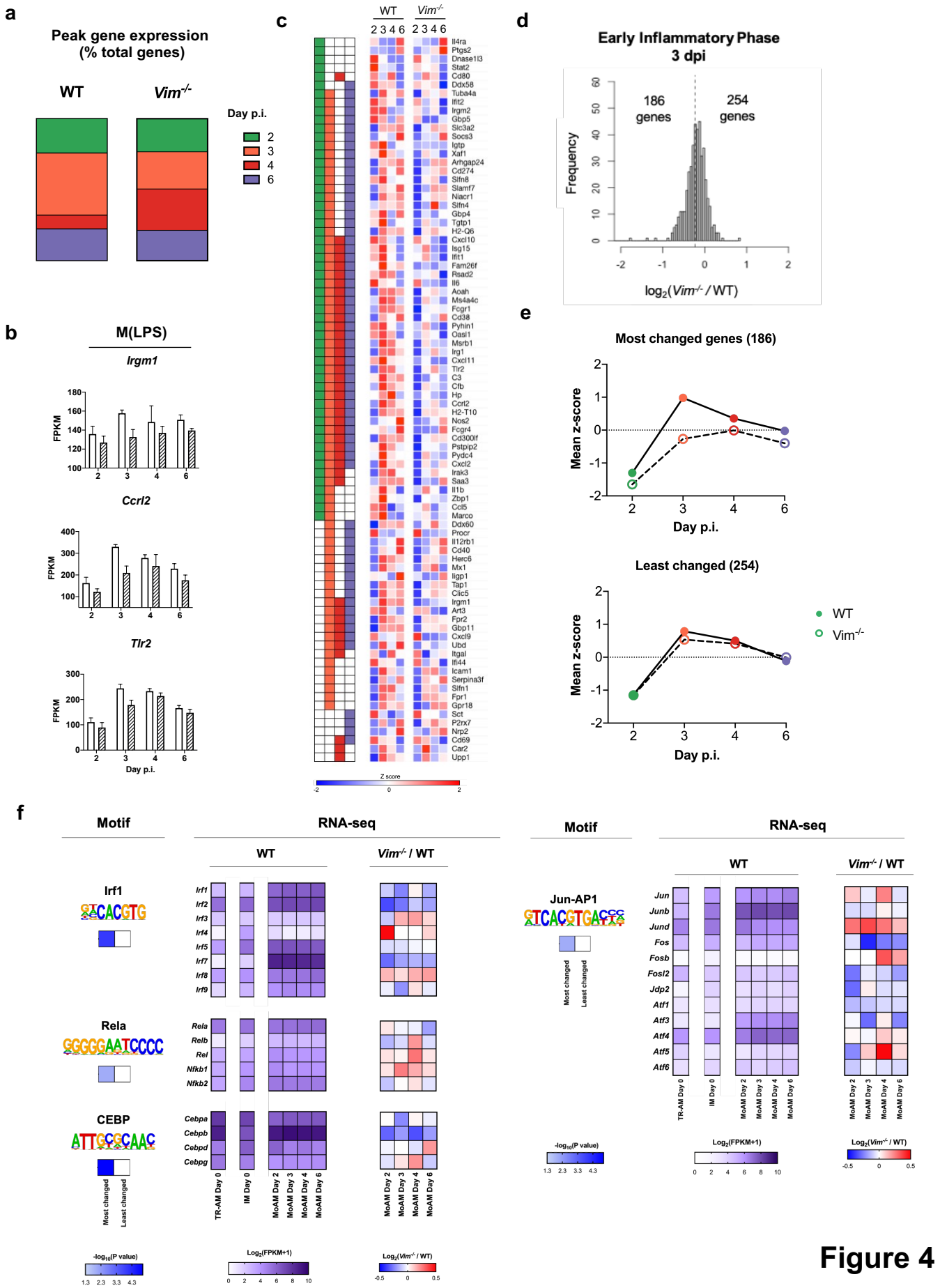
a
Peak gene expression
(% total genes)
WT
Vim-/-
Day p.i.
2
3
4
6
b
M(LPS)
Irgm1
Ccrl2
Tlr2
FPKM
Day p.i.
c
WT
Vim-/-
2 3 4 6
2 3 4 6
Il4ra
Ptgs2
Dnase1l3
Stat2
Cd80
Ddx58
Tuba4a
Ifit2
Irgm2
Gbp5
Slc3a2
Socs3
Igtp
Xaf1
Arhgap24
Cd274
Sifn8
Slamf7
Niacr1
Sifn4
Gbp4
Tgtp1
H2-Q6
Cxcl10
Isg15
Ifit1
Fam26f
Rsad2
Il6
Aoah
Ms4a4c
Fcgr1
Cd38
Pyhin1
Oasl1
Msrb1
Irg1
Cxcl11
Tlr2
C3
Cfb
Hp
Ccrl2
H2-T10
Nos2
Fcgr4
Cd300lf
Pstpip2
Pydc4
Cxcl2
Irak3
Saa3
Il1b
Zbp1
Ccl5
Marco
Ddx60
Procr
Il12rb1
Cd40
Herc6
Mx1
Iigp1
Tap1
Clic5
Irgm1
Art3
Fpr2
Gbp11
Cxcl9
Ubd
Itgal
Ifi44
Icam1
Serpina3f
Sifn1
Fpr1
Gpr18
Sct
P2rx7
Nrp2
Cd69
Car2
Upp1
Z score
d
Early Inflammatory Phase
3 dpi
186
genes
254
genes
Frequency
log2(Vim-/- / WT)
e
Most changed genes (186)
Least changed (254)
Mean z-score
Day p.i.
WT
Vim-/-
f
Motif
RNA-seq
WT
Vim-/- / WT
Irf1
Rela
CEBP
Jun-AP1
Most changed
Least changed
TR-AM Day 0
IM Day 0
MoAM Day 2
MoAM Day 3
MoAM Day 4
MoAM Day 6
-log10(P value)
Log2(FPKM+1)
Log2(Vim-/- / WT)

Figure 4

Supplemental Figure 4

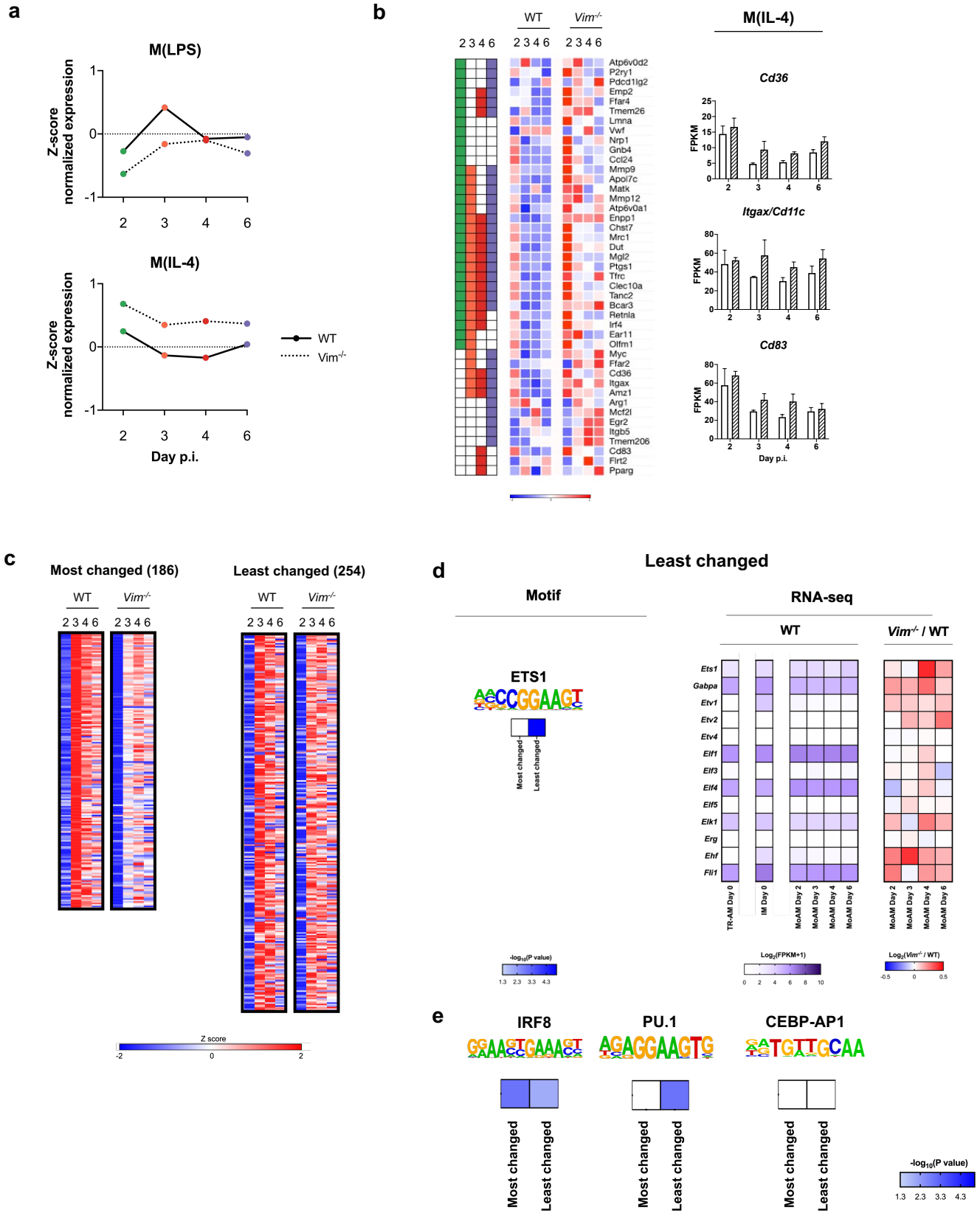

Figure 5

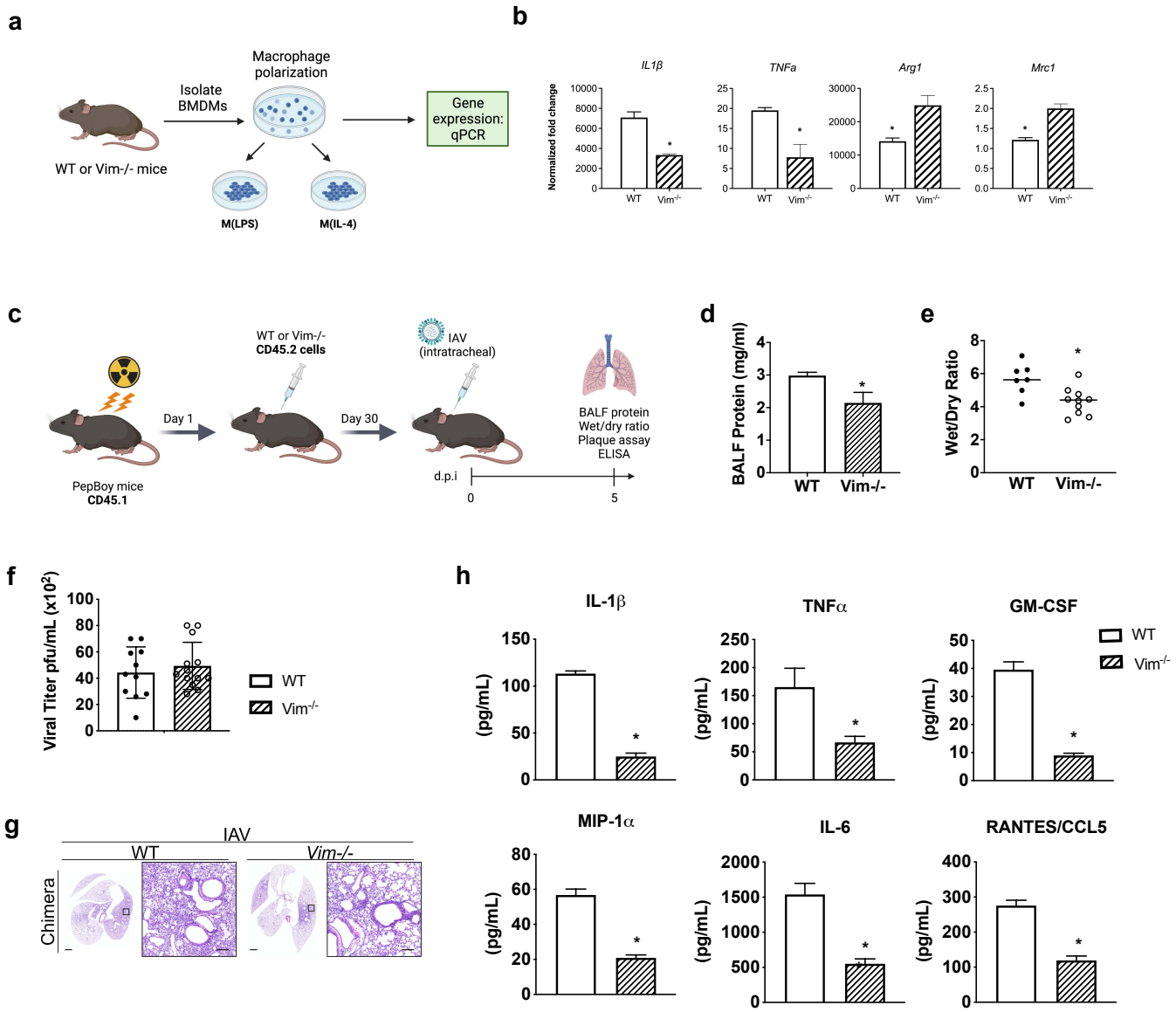
a
Macrophage polarization
Isolate BMDMs
Gene expression: qPCR
WT or Vim-/- mice
M(LPS)
M(IL-4)
b
IL1β
TNFa
Arg1
Mrc1
Normalized fold change
WT
Vim-/-
c
WT or Vim-/- CD45.2 cells
IAV (intratracheal)
Day 1
Day 30
PepBoy mice CD45.1
d.p.i
0
5
BALF protein
Wet/dry ratio
Plaque assay
ELISA
d
BALF Protein (mg/ml)
WT
Vim-/-
e
Wet/Dry Ratio
WT
Vim-/-
f
Viral Titer pfu/mL (x10²)
WT
Vim-/-
g
IAV
WT
Vim-/-
Chimera
h
IL-1β
TNFα
GM-CSF
MIP-1α
IL-6
RANTES/CCL5
(pg/mL)
WT
Vim-/-
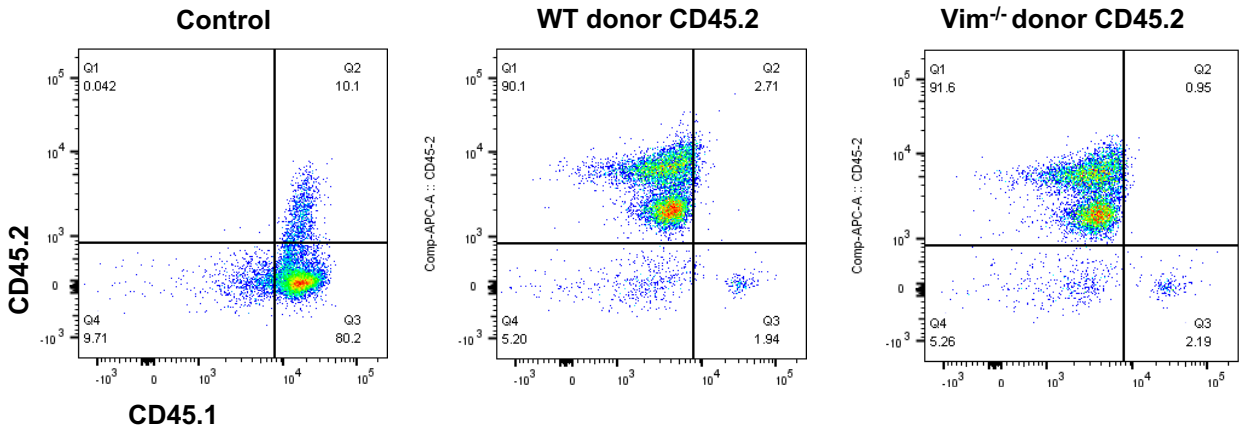
Supplemental Figure 5